Publications

3-31-2011

Cluster Observations of a Cusp Diamagnetic Cavity: Structure, Size, and Dynamics

K. Nykyri
Embry-Riddle Aeronautical University, nykyrik@erau.edu

A. Otto
University of Alaska, Fairbanks

E. Adamson
University of Alaska, Fairbanks

E. Dougal
Embry-Riddle Aeronautical University

J. Mumme
Embry-Riddle Aeronautical University

Follow this and additional works at: https://commons.erau.edu/publication

Part of the Astrophysics and Astronomy Commons

Cluster observations of a cusp diamagnetic cavity: Structure, size, and dynamics

K. Nykyri,[1] A. Otto,[2] E. Adamson,[2] E. Dougal,[1] and J. Mumme[1]

[1]   We have analyzed Cluster magnetic field and plasma data during high-altitude cusp crossing and compared them with high-resolution MHD simulations. Cluster encountered a diamagnetic cavity (DMC) during northward interplanetary magnetic field (IMF) conditions, and as the IMF rotated southward, the spacecraft reencountered the cavity more at the sunward side of the cusp because the reconnection site had changed location. We found evidence of magnetic reconnection both during northward and southward IMF conditions. The Cluster separation was ~5000 km, enabling for the first time measurements both inside the DMC and surrounding boundaries that allowed us to construct the structure of the DMC and put the observations of ion pitch angle distributions in context of local reconnection topology and gradients of the boundaries. The cavity is characterized by strong magnetic field fluctuations and high-energy particles. At the magnetosheath boundary the high-energy particle fluxes reduced by several orders of magnitude. Throughout the magnetosheath, the high-energy proton fluxes remained low except during brief intervals when sc4 and sc1 dropped back into the cavity due to changes in solar wind dynamic pressure. However, the high-energy O+ fluxes did not drop as much in the magnetosheath and were mostly at 60°–120° pitch angles, indicative of a trapped population in the DMC which is observed in the magnetosheath due to a large gyroradius. Significant fluxes of protons and ionized oxygen were also observed escaping from the diamagnetic cavity antiparallel to the magnetic field in a time scale more consistent with the local DMC source than with a reflected bow shock source.

Citation: Nykyri, K., A. Otto, E. Adamson, E. Dougal, and J. Mumme (2011), Cluster observations of a cusp diamagnetic cavity: Structure, size, and dynamics, *J. Geophys. Res.*, *116*, A03228, doi:10.1029/2010JA015897.

1.   Introduction

[2]   The geomagnetic cusps are a key structural elements of the magnetospheric boundary layers and the magnetosheath plasma has the most direct access to the ionosphere through high-altitude cusps [*Heikkilä and Winningham*, 1971; *Frank and Ackerson*, 1971]. Prior to four spacecraft, multi-instrument Cluster mission, in situ measurements of the cusps and high-latitude magnetopause were provided by HEOS, ISEE2, Hawkeye, Polar and Interball missions [e.g., *Paschmann et al.*, 1976; *Gosling et al.*, 1991; *Kessel et al.*, 1996; *Dunlop et al.*, 2000]. Of particular interest has been the identification of lobe reconnection [*Gosling et al.*, 1991; *Kessel et al.*, 1996; *Scudder et al.*, 2002; *Fuselier et al.*, 2000; *Russell et al.*, 2000] and the spatial extent of the cusp [*Zhou et al.*, 1999, 2000]. The cusps also exhibit significant magnetic field fluctuations which can be created by solar wind (bow shock) perturbations, magnetic reconnec-

tion or intrinsic instabilities present in the cusp [*Savin et al.*, 1998; *Chen and Fritz*, 1998; *Le et al.*, 2001; *Savin et al.*, 2002, 2004].

[3]   Cluster has been ideal for studying the high-altitude and midaltitude cusps. Cluster has revealed for the first time many important observational aspects of the structure of the high-altitude cusps, and especially how they are related to the prevailing solar wind and interplanetary magnetic field (IMF) conditions [e.g., *Lavraud and Cargill*, 2005; *Cargill et al.*, 2005; *Lavraud et al.*, 2005a]. For Northward IMF, a picture is emerging of a cusp influenced by lobe reconnection [*Vontrat-Reberac et al.*, 2003; *Twitty et al.*, 2004; *Lavraud et al.*, 2005a] with Earthward directed plasma jets being observed, but also containing regions of stagnant plasma [*Lavraud et al.*, 2002, 2004]. On the other hand, for Southward IMF, the cusp is dominated by tailward convection due to subsolar reconnection [*Cargill et al.*, 2004].

[4]   One particularly interesting aspect of the cusp encounters have been the observations of extensive regions of magnetic field fluctuations seemingly associated with Earthward directed plasma flows generated by lobe reconnection. These flows are observed near the boundary between the cusp and lobe, where the magnetic field is still quite large, ~100–60 nT [*Nykyri et al.*, 2003a, 2004; *Sundkvist*

[1]Department of Physical Sciences, Embry-Riddle Aeronautical University, Daytona Beach, Florida, USA.
[2]Geophysical Institute, University of Alaska Fairbanks, Fairbanks, Alaska, USA.

et al., 2005; *Nykyri et al.*, 2006a]. The level of fluctuations appears to correlate with the magnitude of the flows and the ion number flux, and also shows wave activity with strong peaks at the ion cyclotron frequency. The role that these waves play in heating, scattering and transport is still unclear. The energy level in these waves close to ion cyclotron frequency is small and assuming a complete dissipation of the wave with an amplitude of 5 nT in plasma density of $10/cm^3$, one would expect a temperature increase of 10^5 K which is insignificant compared to measured temperatures in the cusp which are typically 2–10 MK. However, these waves may have sufficient energy to accelerate a small fraction of the distribution. In addition statistical study of the properties of the exterior cusp has shown that the magnetic field fluctuations are closely associated with the magnetic shear angle, which indicates that the large-amplitude fluctuations in the high-latitude exterior cusp region are mainly produced by the high- latitude reconnection process [*Zhang et al.*, 2005]. Our observations of reconnection signatures in the present paper and in the work by *Nykyri et al.* [2011] are in agreement with this result.

[5] Despite these advances, there are still unresolved questions concerning the cusp physics. Probably the biggest is on the origin of cusp energetic particles (CEPs) observed at the high-altitude cusp during intervals of strongly depressed magnetic field [*Chen and Fritz*, 1998]. These regions of depressed magnetic field at high-altitude cusp are called diamagnetic cavities (DMCs) and they are frequently occupied by high-energy particle populations [*Chen and Fritz*, 1998; *Fritz et al.*, 1999; *Chen and Fritz*, 2001; *Zhang et al.*, 2005; *Whitaker et al.*, 2006, 2007; *Walsh et al.*, 2007; *Niehof et al.*, 2008; *Walsh et al.*, 2010]. *Zhang et al.* [2005] showed that high-energy ions above 28 keV are present most of the time while high-energy electrons are less frequent. Currently there are three schools of thought on the origin of these high-energy populations: (1) local acceleration [*Chen and Fritz*, 1998; *Chen*, 2008], (2) bow shock source [*Chang et al.*, 1998, 2000; *Trattner et al.*, 2001], and (3) magnetospheric source [*Sibeck et al.*, 1987; *Fuselier et al.*, 1991; *Kremser et al.*, 1995; *Delcourt and Sauvaud*, 1998; *Lavraud et al.*, 2005b; *Asikainen and Mursula*, 2005, 2006].

[6] *Chen and Fritz* [1998] have suggested that energetic ion populations are generated by acceleration via ULF wave turbulence present in DMCs. In order to understand the physical mechanisms that could accelerate the ions in the cusp one needs first to identify what is the "turbulence" in the DMCs. We demonstrate in this paper and in the work by *Nykyri et al.* [2011] that what looks like "turbulence" in the time series is in fact mostly motion of the structure by spacecraft.

[7] Our motivation for the present study has been to identify the source for the high-energy particles in the cusp diamagnetic cavity and obtain a better understanding of reconnection dynamics, structure, fluctuations in the cavity, formation and re-formation of the cavity for changing IMF orientation, and properties of ion distribution functions and high-energy particles in relation to cavity boundaries. In order to find an event with simultaneous measurements in the cavity and surrounding magnetosheath we searched through Cluster spacecraft orbits between 2001 and 2005 in order to find a perfect event where the IMF changes from northward to southward and spacecraft separation is large

enough to study plasma properties simultaneously in the DMC and in the magnetosheath.

[8] Our survey indicates that Cluster encountered clear DMCs only when the dynamic pressure of the solar wind was high enough (typically above ~2 nPa). During many (about one third) of the high-altitude cusp crossings Cluster observes a magnetic field that is not depressed like during DMCs but gradually decreases from ~100 nT to ~20 nT. This is due to the Cluster orbit. For Polar spacecraft, that observes DMCs most of the time during high-altitude cusp crossing and for extended time periods, the DMC is in the apogee of the orbit so Polar moves very slowly through this region. Cluster moves faster through this region and at lower altitude during part of the orbit, so it only "sees" clear diamagnetic cavity during intervals of enhanced dynamic pressure.

[9] We have divided the material of this study into three papers. The present paper discusses the structure, size and dynamics of cusp diamagnetic cavity, the second paper focuses on analysis of the magnetic field fluctuations in the DMC [*Nykyri et al.*, 2011], and the third paper discusses the high-energy particle observations in the DMC (K. Nykyri et al., On the origin of high-energy particles in cusp diamagnetic cavity, submitted to *Journal of Geophysical Research*, 2010). In order to explain the high-energy particle observations a good understanding of reconnection structure, dynamics and boundary normal orientations is needed.

[10] The paper is organized as follows. Section 2 describes the instrumentation and data analysis tools, section 3 discusses an overview of the event, section 4 describes the reconnection dynamics and observations, section 5 describes the structure of the cavity and analysis of "sheath intervals" that show presence of high-energy particles, section 6 concludes the study and Appendix A illustrates the method used in determination of stability and error estimates of the boundary normals that are used in determining the size and orientation of the boundaries in the DMC.

2. Instrumentation and Data Analysis Tools

[11] We use data from four instruments on Cluster. From each spacecraft, we use magnetic field measurements from the Flux Gate Magnetometer (FGM) [*Balogh et al.*, 2001], with a sampling rate of 4 vectors/s; ion spectra and moments from the Cluster Ion Spectrometer (CIS) [*Rème et al.*, 2001] from spacecraft 1 (sc1), 3 (sc3) and 4 (sc4) and energetic particle data from RAPID (Research with Adaptive Particle Imaging Detectors) spectrometer [*Wilken et al.*, 2001]. We use 4 s time resolution data for temperature, velocity and density from the Hot Ion Analyzes (HIA) on sc1 and sc3. The HIA data has some data gaps that are linearly interpolated. The longest (shortest) data gaps are 48 s (4 s) in duration. The proton velocity, temperature and densities for sc4 are obtained from the ion Composition and Distribution Function analyzer (CODIF) for every 4 s and 8 s during some intervals. Our data analysis tools use the de Hoffman–Teller (HT) analysis and the Walén relation [*Sonnerup et al.*, 1995]. The HT frame is a frame where the convection electric field vanishes, thus indicating an approximately steady state plasma configuration. The electric field for the HT plots is calculated from $-\mathbf{v_{obs}} \times \mathbf{b_{obs}}$, where $\mathbf{b_{obs}}$ and $\mathbf{v_{obs}}$ are obtained from FGM and CIS data, respectively. The HT
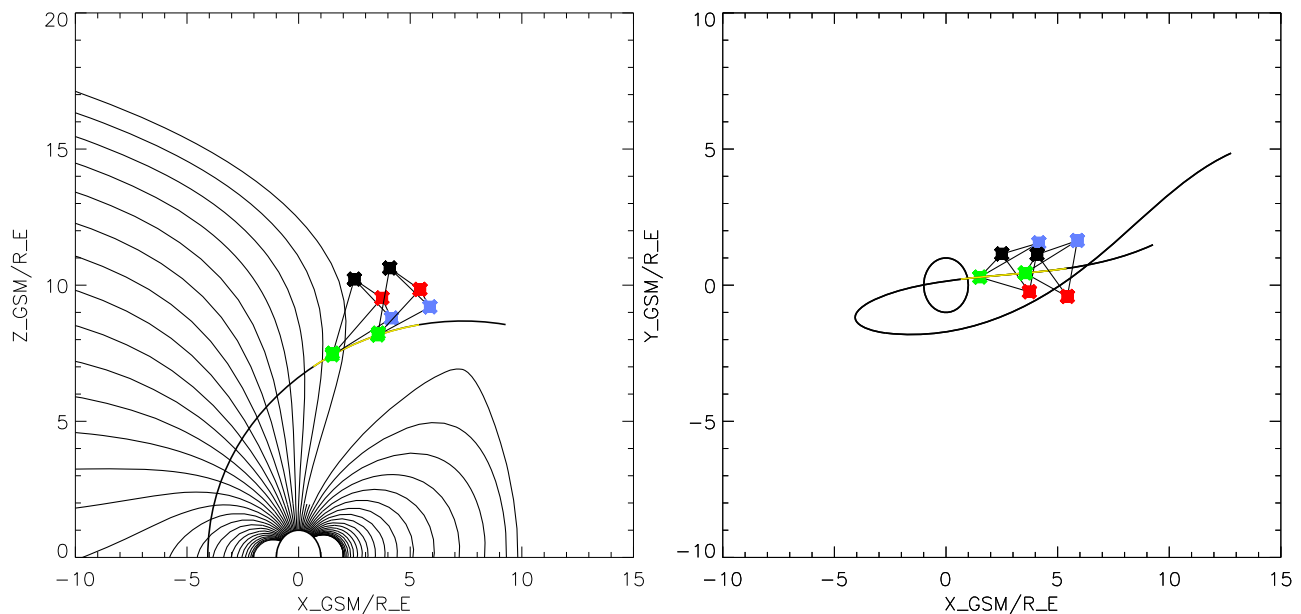
Figure 1. (left) Cluster trajectory on 14 February 2003 plotted on top of the magnetic field lines from Tsyganenko 89 model (T89) in GSM coordinates in *xz* plane and (right) trajectory and constellation plotted in *xy* plane. The T89 model uses the *Kp* index of 4. The circle is the Earth, the yellow line depicts Cluster trajectory between 1800 and 2100 UT, and Cluster constellation (magnified by factor of 3) is drawn with respect to sc3 position at 1830 UT and at 1945 UT.

velocity, $\mathbf{v_{HT}}$, is determined by minimizing $|(\mathbf{v} - \mathbf{v_{obs}}) \times \mathbf{b_{obs}}|^2$ in terms of the constant transformation velocity $\mathbf{v}$ for a given data set [*Sonnerup et al.*, 1995]. In order to obtain a slope for the HT frame a linear least squares fit is calculated for the data set: electric field components on the *y* axis and HT electric field on the *x* axis.

[12] The Walén relation is calculated in the HT frame as $\mathbf{v} - \mathbf{v_{HT}} = \pm C \, \mathbf{v_A}$ and implies that in the HT frame the plasma flow velocity is Alfvénic [*Sonnerup et al.*, 1995]. The Alfvén velocity, $\mathbf{v}_A = \mathbf{B}/\sqrt{(\mu_0 n_p m_p)}$, is corrected by factor $C = \sqrt{(1 - \alpha)}$, where $\alpha = (T_\| - T_\perp)n_p k_B \mu_0/B^2$ is the pressure anisotropy correction [e.g., *Sonnerup et al.*, 1981]. The Walén relation is satisfied for Alfvén waves, rotational discontinuities, but also approximately for intermediate and switch-off slow shocks. These phenomena are often associated with magnetic reconnection.

[13] The boundary normal directions are calculated using the minimum variance of the magnetic field (MVAB), maximum variance of the electric field (MVAE) [*Sonnerup and Scheible*, 1998] and Minimum Faraday Residue (MFR) method [*Khrabrov and Sonnerup*, 1998]. *Haaland et al.* [2004] used MFR method and compared it with other single-spacecraft and multispacecraft methods for the magnetopause event. They found that multispacecraft technique Constant Thickness Approach (CTA) and a hybrid technique CTAM gave reasonably good agreement (≈5°) with MFR method. For our event, the dominant magnetic field and the dominant plasma velocity are tangential to the boundary layer such that the maximum variance for the convection electric field should be normal to the layer.

3. Overview of the Cusp Encounter

[14] The DMC crossings are on the outbound leg of Cluster orbit in the Northern hemisphere at ~8 R_E altitude. Cluster trajectory and constellation (magnified by factor of 3) in GSM coordinates are presented in Figure 1. Cluster spacecraft separation is ~5000 km enabling simultaneous multipoint observations of plasma and magnetic field properties both inside and outside the cusp DMC. Spacecraft 4 (sc4 hereafter) is leading the constellation (blue), followed by sc2 (red), sc1 (black) and sc3 (green).

[15] The overview of the Cluster observations between 1830 and 2030 UT on 14 February 2003 is presented in Figure 2. The measurements of spacecraft 1, 2, 3 and 4 are marked with black, red, green and blue, respectively. The plasma observations show ion number density (Figure 2a), three components of the ion velocity (Figures 2b–2d), total ion velocity (Figure 2e), and ion temperature (Figure 2f). The magnetic field components and total magnetic field

Figure 2. Cluster (a–f) plasma and (g–j) magnetic field observations on 14 February 2003. Also shown are Cluster separation (units are in thousands of kilometers) from sc3 projected at (l) *xy* plane and (m) *xz* plane and Cluster location (units are in Earth radius) at (n) *xy* plane and (o) *xz* plane. The approximate magnetopause and bow shock locations are drawn as parabolas. (k) The dynamic pressure of the solar wind (orange line) and the three components of the IMF measured by ACE spacecraft lagged by 44.0 min are shown with black, red, and blue corresponding to *x*, *y*, and *z* components, respectively.
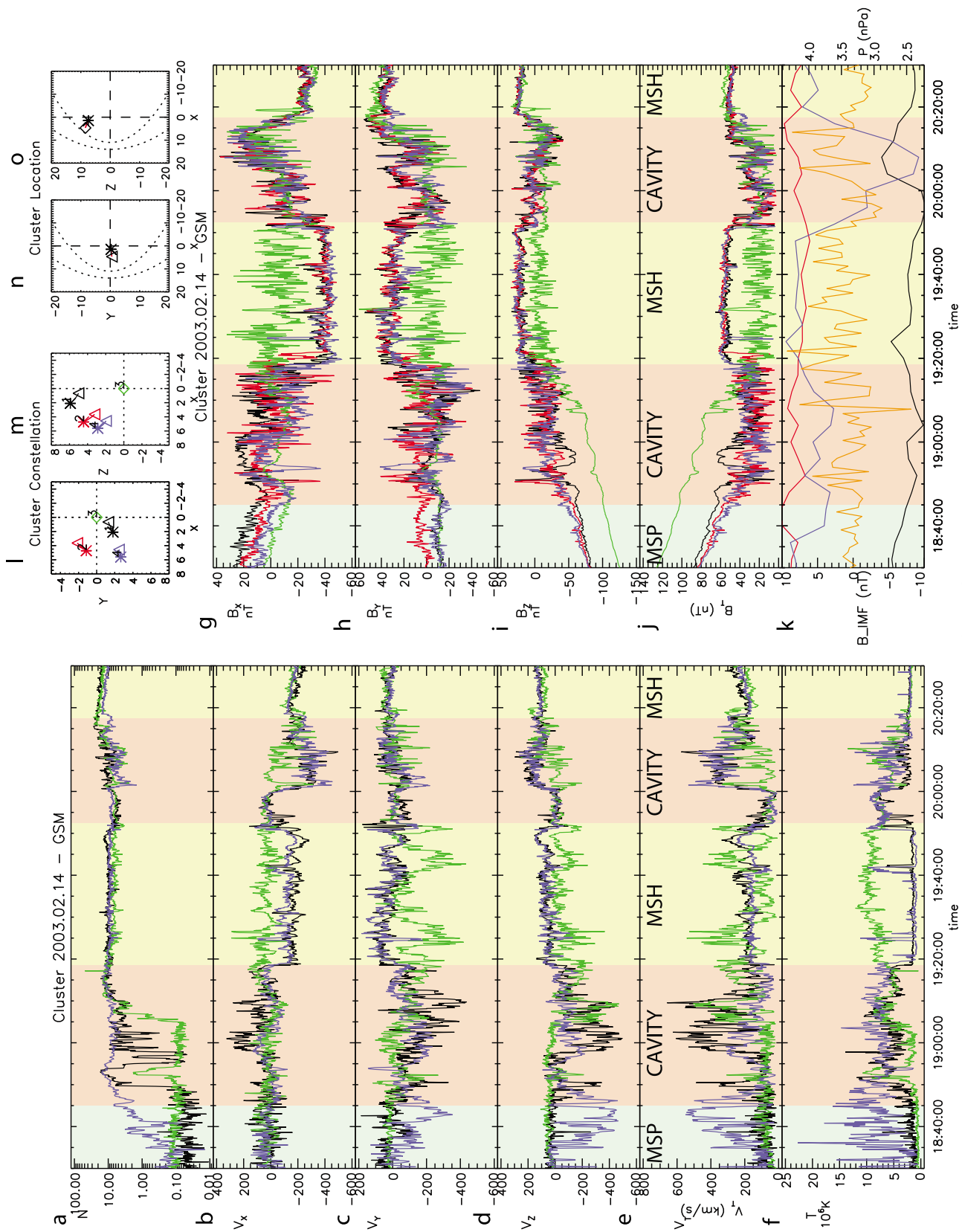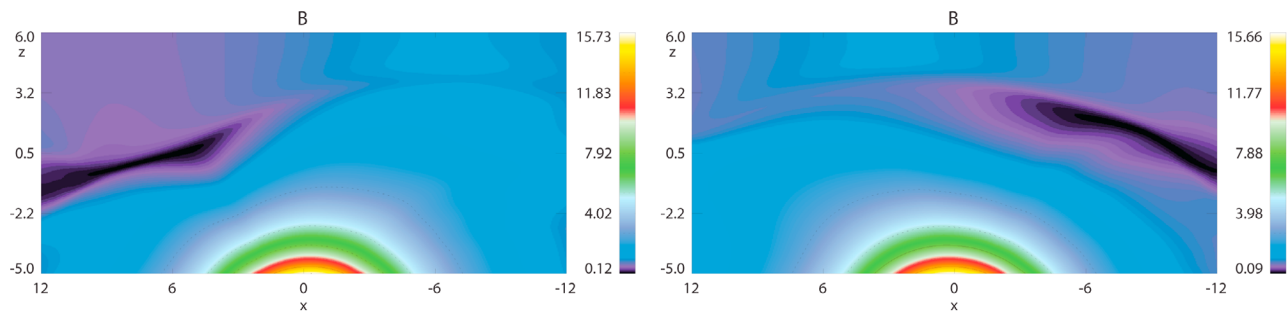
Figure 2

Figure 3. MHD simulations of the cusp for (left) southward and (right) northward IMF. Sun is to the left. Background color is the total magnetic field strength. The region of depressed magnetic field (cavity) is forming more sunward when IMF is southward.

measured by Cluster are plotted in Figures 2g–2j. Three components of the interplanetary magnetic field (IMF) (b_x, b_y, and b_z are marked with black, red, and blue, respectively) and dynamic pressure (orange line) measured by ACE spacecraft and lagged by 44.0 min are plotted in Figure 2k. Initial time lag is calculated between 1830 and 2030 UT from $\Delta t = \Delta x / \langle v_x \rangle$ where Δx is the distance between ACE and Cluster along x-direction and $\langle v_x \rangle$ is the average of the x component of the solar wind speed. This gives a time lag of ~49.1 min. This procedure is repeated for the ACE data that has been shifted by 49.1 min and this gives a new time lag of 48.9 min, which indicates that there was no big discontinuity in solar wind speed between 1741 and 2030 UT. The v_x in the solar wind during this shifted 2 h interval varies between ~−455 km/s and −515 km/s which can cause a difference of ~6 min in time lag estimates. We have used the time lag of 44 min in order to better match the main features in the Cluster data.

[16] The lagged ACE data indicates that the IMF was strongly northward up to 1948 UT, after which it starts to rotate southward reaching −9 nT at 2006 UT. The IMF returns back northward reaching 7 nT by ~2019 UT. The solar wind speed (not shown) is ~500 km/s and the dynamic pressure varies between 2.5 and 4.3 nPa.

[17] The transition from the tail lobe magnetosphere (MSP) to the DMC is characterized by an increase of plasma density, enhanced magnetic field fluctuations, depressed total magnetic field, appearance of large field aligned plasma flows associated with lobe reconnection during prevailing northward IMF conditions and enhanced plasma temperature. Note that the cavity region is more pronounced here and the observed plasma temperatures are much higher than for the cusp crossing reported by *Lavraud et al.* [2002], which occurred during a low dynamic pressure of the solar wind. They also did not report any observations of high-energy particles during this crossing.

[18] This transition from MSP to DMC occurs first for sc4 between 1830 and 1850 UT, followed by sc1 at 1850 UT and finally by sc3 at 1905 UT. There are no CIS measurements for sc2, but based on the magnetic field signatures, the transition to diamagnetic cavity occurs slightly earlier for sc2 than for sc1. This can be most easily seen as a sharp decrease of total magnetic field at 1850 UT (at sc2) and at 1851 UT (at sc1). Based on the density measurements, the transition from MSP to cusp is gradual at sc4, but is more

abrupt at sc1 and at sc3. One can also notice that sc1 returns briefly back to the MSP at ~1855 UT before finally returning back to the cavity. This is produced by back and forth motion of the cavity boundary by sc1 due to dynamic pressure variations [*Nykyri et al.*, 2011].

[19] Sc1 and sc4 are in the cavity until ~1918 UT after which they move to the magnetosheath. The transition into magnetosheath is probably mostly produced by dynamic pressure enhancement in the solar wind: during the first magnetosheath interval the average level of the dynamic pressure is higher than during the cavity intervals. The sharp pressure enhancement at 1917–1918 UT seem to be associated with sc1 and sc4 transition into magnetosheath which is followed by another pressure enhancement 1921–1922 UT which may be associated with sc2 transition into magnetosheath. The transition into magnetosheath may also be associated with the slight change in reconnection site because b_z is increased from previous cavity interval and the spacecraft have moved further sunward. For more northward IMF the cavity is formed more tailward (see later discussion of Figure 3) which could partly explain (together with dynamic pressure enhancement) why three of the spacecraft move into magnetosheath. Note that sc3 remains in the cavity because it is furthest tailward but is also furthest away from magnetosheath along z direction (is deepest in the cavity), so pressure variation does not move it into magnetosheath compared to those spacecraft that have a higher z coordinate. Evidence for the change of reconnection site may be the fast flows observed by sc3 at ~1925 UT. The magnetosheath is characterized by a steady tailward ion velocity (negative v_x), decreased ion temperature and increased magnetic field. The draping of the IMF around the magnetopause generates a strong negative b_x in the magnetosheath.

[20] The lagged ACE data shows that IMF starts to rotate from northward to southward at ~1948 UT which is also accompanied by the dynamic pressure decrease of 40%. The change of the reconnection site and dynamic pressure decrease can cause a motion of magnetopause and cavity boundaries such that sc1, sc2 and sc4 reencounter the region of the depressed field. It seems that the transition into cavity is mostly due to changing IMF because the subsequent pressure increase that starts at ~2000 UT is not adequate to move the spacecraft back into magnetosheath. The change of the reconnection site is further demonstrated with Walén relations and de Hoffman–Teller frame velocities in section 4.
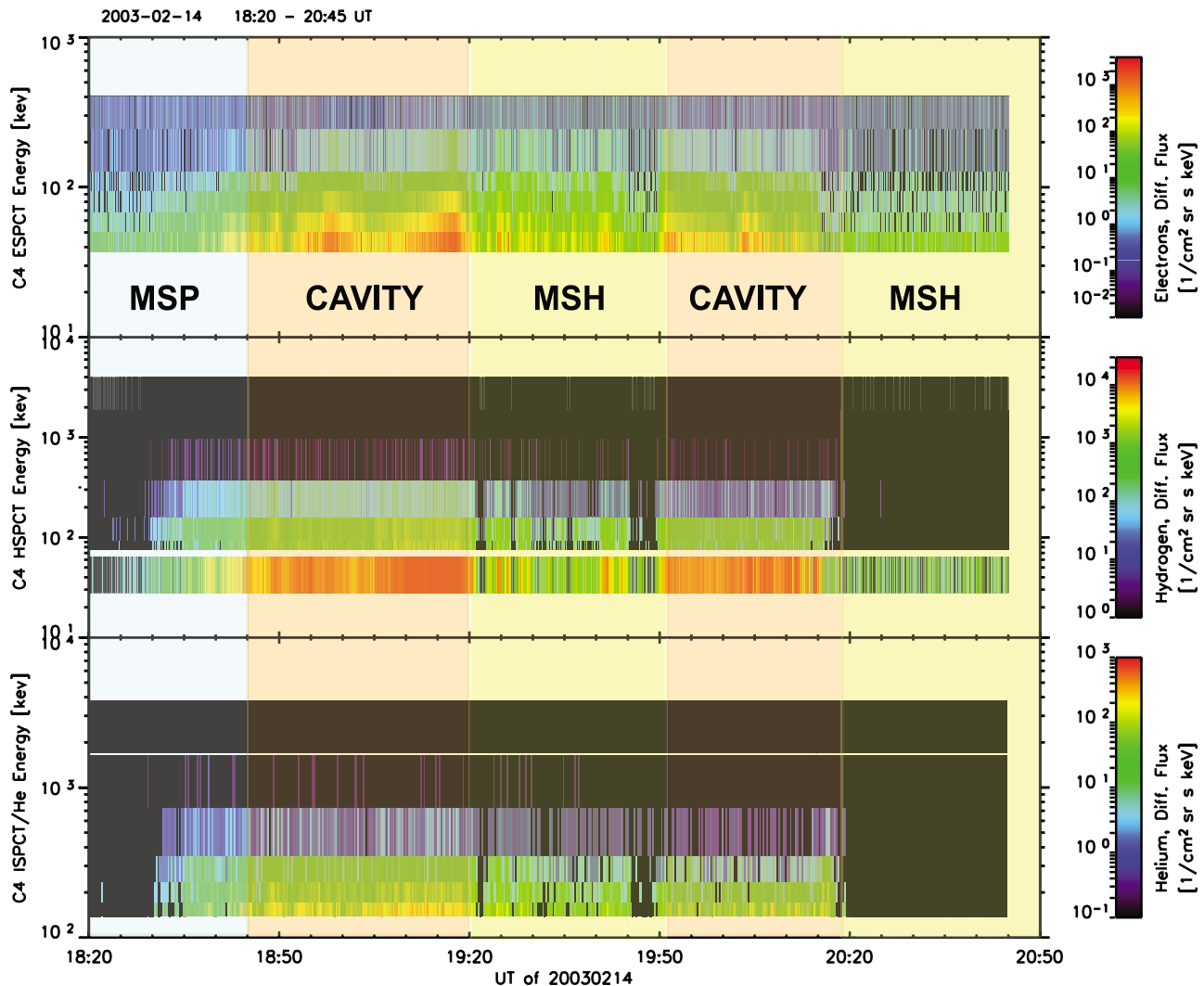
Figure 4. Sc4 measurements of (top) electron, (middle) proton, and (bottom) helium omnidirectional fluxes at different energies between 1820 and 2045 UT.

[21] The last transition into magnetosheath seems to be associated with both: the sharp pressure increase at ~2014 UT and the change of b_z from southward to zero. Note that when pressure reduces by 2015 UT, sc4 which is closest to cavity boundary drops back to weak field region but finally returns back to magnetosheath as the IMF has rotated more northward. During this strong northward IMF the cavity has moved so much tailward that even the large pressure decrease after 2018 UT is not adequate to bring the spacecraft back into cavity.

[22] We have used high-resolution local MHD cusp model (E. Adamson et al., 3-D mesoscale MHD simulations of a cusp-like magnetic configuration: Method and first results, submitted to *Annales Geophysicae*, 2010; E. Adamson et al., 3D mesoscale MHD simulations of magnetospheric cusp-like magnetic configurations: Cusp diamagnetic cavities and boundary structure, submitted to *Annales Geophysicae*, 2010) in order to see how the DMC depends on IMF orientation. Figure 3 presents simulation results for northward (Figure 3, right) and southward (Figure 3, left) IMF orien-

tation. The background color is magnetic field strength and Sun is to the left. One can see that the region of depressed field is forming more sunward for southward IMF compared to northward IMF orientation. This can be explained by reconnection site changing location when IMF b_z turns from northward to southward. Note that these results are presented in simulation coordinates. Qualitatively this movement of DMC sunward with southward turning IMF agrees with the Cluster observations. Numerous studies have shown the motion of the cusp sunward with southward IMF in observations [*Burch*, 1973; *Newell and Meng*, 1987; *Palmroth et al.*, 2001b; *Pitout et al.*, 2006; *Niehof et al.*, 2010] and in global MHD simulations [*Palmroth et al.*, 2001a]. In our event sc3 remains in the cavity the entire time so the re-formed cavity must overlap with the original one that was formed during $b_z > 0$.

[23] Energy-time spectrograms of the high-energy particles measured by sc4 are presented in Figure 4. Shown are omnidirectional fluxes of electrons (Figure 4, top), protons (Figure 4, middle), and helium ions (Figure 4, bottom).

Table 1. Properties of Reconnection Intervals Between 1853 and 1925 UT

Interval (UT)	Decimal Hour	Sc	Walén Slope	Walén Correlation Coefficient	HT Slope	HT Correlation Coefficient	HT Velocity (km/s)
1853:20–1853:38	18.8890–18.8940	4	1.01	0.99	0.90	0.96	[96, −199, −1]
1856:30–1856:54	18.9417–18.9484	4	0.86	1.00	0.96	0.98	[9, −60, 25]
1859:15–1859:34	18.9875–18.9930	1	0.81	0.99	0.95	0.98	[−39, −153, −15]
1859:45–1859:57	18.9960–18.9993	1	0.85	0.97	1.00	1.00	[51, −35, 44]
1901:48–1901:59	19.0300–19.0333	1	0.87	0.97	0.91	0.94	[52, −106, −57]
1902:56–1903:11	19.0490–19.0533	1	0.96	0.96	0.94	0.98	[53, −218, −30]
1903:14–1903:26	19.0540–19.0573	1	1.10	0.97	0.93	0.96	[87, −349, −223]
1905:16–1905:35	19.0880–19.0933	4	1.01	0.99	0.98	0.99	[77, −41, 197]
1905:27–1905:39	19.0910–19.0943	1	0.82	0.94	0.97	0.98	[30, −161, −67]
1906:28–1906:40	19.1080–19.1113	1	0.81	0.96	0.97	0.99	[8, −114, 19]
1906:43–1907:04	19.1120–19.1180	4	0.86	0.99	0.99	1.00	[93, 3, 74]
1907:19–1907:44	19.1222–19.1289	1	0.72	0.92	0.84	0.91	[70, −130, −84]
1907:44–1908:00	19.1290–19.1334	4	0.88	0.99	0.98	0.99	[62, −10, 7]
1907:44–1907:56	19.1290–19.1323	1	0.82	0.99	0.92	0.96	[36, −123, −12]
1908:16–1908:32	19.1380–19.1424	4	1.08	0.98	0.95	0.98	[138, −17, 132]
1908:38–1908:50	19.1440–19.1473	1	0.92	0.99	0.99	0.99	[93, −215, −18]
1908:49–1909:07	19.1470–19.1520	1	0.94	0.91	0.96	0.98	[8, −240, 6]
1909:21–1909:33	19.1560–19.1593	1	0.82	0.99	0.96	0.99	[97, −218, −142]
1908:50–1909:34	19.1474–19.1598	1	0.89	0.94	0.87	0.96	[37, −216, −96]
1911:27–1911:39	19.1910–19.1943	1	0.98	0.97	0.94	0.96	[−32, −262, 91]
1915:12–1915:24	19.2536–19.2569	3	0.99	0.99	0.97	0.99	[60, −73, −14]
1917:45–1918:09	19.2960–19.3027	3	0.93	0.99	0.96	0.97	[62, −107, −33]
1917:48–1918:12	19.2967–19.3034	3	0.98	0.99	0.95	0.97	[60, −106, −32]
1919:37–1919:52	19.3270–19.3313	1	0.80	1.00	0.96	0.98	[47, −162, 25]
1923:53–1924:24	19.3981–19.4069	3	0.75	0.94	0.95	0.97	[46, −208, −46]
1924:07–1925:42	19.4020–19.4286	1	0.92	1.00	0.87	0.93	[91, −166, −86]
1924:16–1924:29	19.4047–19.4081	4	0.90	1.00	0.81	0.90	[213, −113, −55]
1924:59–1925:27	19.4164–19.4242	1	0.95	1.00	0.87	0.93	[106, −164, −95]

Comparison of Figure 4 with the total magnetic field measurements shown in Figure 2 reveals that the high-energy particles up to few hundred keV are present during the intervals with depressed magnetic field. The spacecraft have also brief reencounters with the cavity-like plasma and high-energy particles during the "sheath" intervals. An example of such interval can be seen between 1945 and 1950 UT at sc4 (also sc1 reencounters the cavity during this interval (not shown)).

[24] We have found several reconnection intervals with good HT frames satisfying the Walén relation for both northward and southward IMF orientation. In section 4 we will discuss the reconnection geometry and search for reconnection intervals in more detail.

4. Fluid and Particle Evidence for Magnetic Reconnection

[25] We have automated the search for reconnection intervals by applying a sliding window over the data between 1830–2030 UT and testing for a reconnection criteria. In order to ensure that we find most of the reconnection intervals, we have used window sizes of 90, 80, 70, 60, 54, 48, 42, 36, 30, 24, 18 and 12 s. A 6 s sliding is used for 30–90 s searches and a 4 s sliding for 12–24 s searches. We have required that the Walén slopes are between 0.7 and 1.1 for 30–90 s search intervals and between 0.8 and 1.1 for 12–24 s search intervals, and that HT frame slopes are between 0.8 and 1.2. In addition we have required that the correlation coefficients for both tests are at least 0.9. The scatter plots, hodograms, and ion distribution functions of the search results are then examined. Because the data sampling frequency is 4 s, and magnetic field and plasma data is inter-

polated before calculating Walén relation and HT frame velocity, some interval lengths recorded in Tables 1 and 2 can be few seconds shorter or longer than length of the search window size. We have recorded information of the good reconnection intervals into Tables 1 and 2 and have eliminated those intervals from Tables 1 and 2 that had a longer-duration data gap. If a 48 s window is embedded inside a 54 s window, so that both of these satisfy the search criteria, we have recorded the information of the interval having the better slopes and less scatter in Walén and HT frame plots into Tables 1 and 2. In case two intervals are partially overlapping, we have recorded information of the both. We have applied this search method for reconnection intervals before at the low-latitude boundary layer [*Nykyri et al.*, 2006b].

4.1. Reconnection Signatures During Northward IMF
4.1.1. de Hoffman–Teller Frame Velocities and Slopes of the Walén Relations

[26] One typical feature that Tables 1 and 2 show is that most intervals during the first period of northward IMF (intervals up to ~1958 UT) have HT velocities with positive v_x component, negative v_y component, and negative v_z component, and most of the intervals during southward IMF (intervals between 1958 and 2015 UT) have HT velocities with negative v_x and v_y components, and positive v_z components. The last two intervals after 2015 UT are again during northward IMF but have negative v_x components and positive v_y components of the HT velocity. These HT velocities can be explained by the motion of the reconnected flux tubes originating from different reconnection sites surrounding the cusp funnel. Up to 1958 UT and after 2015 UT the IMF is northward and duskward (corresponding to a clock angle

of ~45°) and has a strong negative b_x component, generating a region of largest magnetic shear at the tailward-duskside northern cusp. Reconnection in this geometry will result in two flux tubes moving approximately in opposite directions: one moving sunward and dawnward with positive v_y and negative v_y (type A), and another moving tailward and duskward with negative v_x and positive v_y (type B). The most intervals observed up to 1958 UT are type A. All intervals after 2015 UT have the slopes and v_x and v_y components consistent with type B reconnection, but the very large v_z and the spacecraft location are not consistent with type B lobe reconnection (see more discussion in section 4.3).

[27] The v_z components of the HT velocities for the type A intervals are mostly negative, although there are few intervals where they are positive. The angle between dipole tilt and z_{GSM} axis is $-3°$ at 1830 UT so the dipole points away from the Sun, which together with the fact that dynamic pressure is high and variable may explain the observed positive v_z components during some of the type A events: a pressure pulse can locally compress the magnetopause generating a magnetic tension force with positive z component. This may also depend on what altitude the spacecraft are crossing the flux tube and how "fresh" (e.g., how long ago it has reconnected) the flux tube is. For example, sc4 observes a HT velocity of [77, −41, 197] km/s at 1905–1906 UT when the SW dynamic pressure (shown in Figure 2), P_{dyn}, increases by 10%. P_{dyn} actually shows even larger 75% variations between 1906 and 1909 UT. Considering that solar wind v_x is also varying between −515 km and −455 km, some inaccuracies (order of 2–3 min) will follow when average solar wind speed is used in time lag estimation, so that this signature may be associated with the 75% pressure variation.

[28] The slopes of the Walén relations depend on from which side of the x line the spacecraft cross the reconnected flux tube. Crossing (or partial crossing) of the sunward moving flux tube originating from lobe reconnection (type A) would result in a positive slope, since the normal component of plasma velocity, v_N, and magnetic field, b_N, have the same sign. Most of the intervals have positive slopes during northward IMF.

4.1.2. Example of the Reconnection Interval During Northward IMF

[29] An example of a typical reconnection interval during northward IMF measured by sc1 is shown in Figure 5. Figure 5a is in the same format as Figure 2 and shows plasma (Figure 5a, left) and magnetic field (Figure 5a, right) observations between 1906 and 1912 UT. A cartoon in Figure 6a shows how sc1 might be crossing the reconnected flux tube in xz plane in order to explain the observed signatures in magnetic field and ion distribution functions (see caption of Figure 6 for more details). The highlighted column in Figure 5 depicts a 44 s time interval measured by sc1 satisfying the reconnection criteria. Because the flow in the magnetosheath is sub-Alfvénic and the IMF orientation is quite steady during 1906–1912 UT, the reconnection is occurring somewhat continuously generating flux tubes moving earthward and dawnward (type A) and tailward and duskside (type B). The observed HT frame velocity has the strongest $-y$ component, ~−200 km/s, positive v_x and negative v_z, which is a signature of type A flux tube. During the 44 s, a single flux tube moves earthward a distance of $V_{HT} \cdot$

44 s = ~1.65 R_E (probably feeling some resistance by the magnetosheath flow), so it is likely that several reconnected flux tubes are swept by sc1 during this interval.

[30] Figure 6a shows a cartoon of a time history of reconnected field lines ("1" refers to field line that reconnected first and "3" refers to a field line that is just reconnecting) and relative trajectory of sc1 with respect to reconnected flux tubes; the curve labeled c–f refers to measured distribution functions in Figure 5. The ion distribution functions (Figures 5c–5f) show most flux in quadrants 1 and 2 (numbering scheme for quadrants is illustrated in Figure 5c), indicating that particles are moving parallel to magnetic field and that the mirrored population is absent, which indicates that field lines are freshly reconnected. Eventually the sunward motion of the reconnected field lines gets reduced, which may explain the relatively small v_x component during the beginning of the interval and some reflected particles in the ion distribution functions in Figures 5c–5e. As sc1 crosses more freshly reconnected field lines the v_x increases to 275 km/s and simultaneously the b_x rotates from −7 to 15 nT. One should also remember that the reconnection is happening at the duskside of the cusp so the actual motion of the field lines has the largest $-y$ component. Finally we would like to note that highly variable dynamic pressure of the solar wind will make this entire region to oscillate in a time scale of 3–5 min, which would also result in relative motion of the reconnected flux tubes by the spacecraft. However, the b_z and b_y remain negative during this interval, so sc1 is not crossing into the magnetosheath side of the reconnected flux tube where the b_z and b_y should be positive for the prevailing draping geometry of the IMF. This is also consistent with the absence of antiparallel ion population in the distribution function in Figure 5f.

[31] A larger interval around the interval in Figure 5 from 1908:36 to 1910:12 UT also yields a reasonable Walén relation with a positive slope of 0.74 and HT frame of 0.89. The MVAB and MFR tests show a hodogram that is a mirror image of letter "S" and MVAE test shows a "S" shaped hodogram (see Figure 7 and caption for more details). The S-shaped hodograms have been observed at the magnetopause [Berchem and Russell, 1982], and could be associated with the Alfvén (intermediate) shocks [Lyu and Kan, 1989].

4.2. Reconnection Signatures During Southward IMF

4.2.1. The de Hoffman–Teller Frame Velocities and Slopes of the Walén Relations

[32] Between 1954 and 2015 UT, the IMF remained duskward and IMF b_z turns gradually from 0 nT to −10 nT and then gradually back up to 0 nT. When the IMF clock angle becomes 135°, the most antiparallel region forms at sunward, duskside cusp, so the reconnection site is expected to move from duskside cusp (approximate location during $b_z \sim 0$ nT) further sunward (in MLT). Table 2 indicates that the HT velocities change and increase after 2004 UT compared to two intervals observed by sc4 at ~2000 and 2001 UT when b_z is closer to zero. These changing HT velocities are likely to be evidence for reconnection site moving sunward. However, throughout 1954–2015 UT, the reconnection region remains somewhere between duskside-sunward cusp. In this geometry the reconnected flux tubes will move

Figure 5. (a) Plots of (left) plasma and (right) magnetic field observations between 1906 and 1912 UT during northward IMF. (b) Walén relations and HT frames during the highlighted interval between 1908:50 and 1909:34 UT (19.1474 and 19.1596 UT) measured by sc1. (c–f) Evolution of the ion distribution functions measured by sc1 in parallel-perpendicular plane between 1908:50 and 1909:27 UT.

tailward and dawnward (type C), and duskward and sunward (type D). Table 2 indicates that nearly all of the intervals between 1958 and 2015 UT have HT velocities consistent with type C reconnection (see discussion on abnormalities in section 4.3).

4.2.2. Example of the Reconnection Interval During Southward IMF

[33] Figure 8 is in same format as Figure 5 and shows a typical example of a reconnection interval (type C) between 2007:40 and 2008:00 UT measured by sc3 during south-
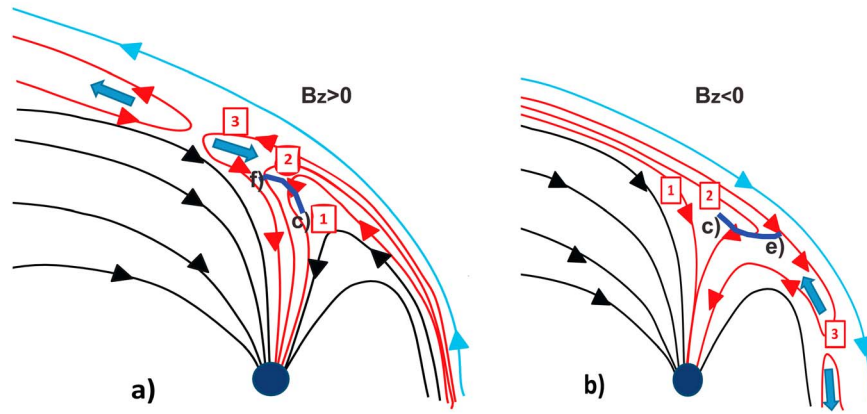
Figure 6. Cartoons of reconnection topology (a) during northward IMF and (b) during southward IMF. The blue line is the solar wind magnetic field line, the red lines are reconnected field lines, and black lines depict closed magnetic field lines. Numbering shows the time sequence of the events, where 1 refers to a field line that reconnected first and 3 refers to a field line that is just reconnecting. The purple curves labeled c–f and c–e illustrate how the spacecraft might be moving relative to reconnected field lines in order to explain the observed HT frame velocities, magnetic and velocity fields, and ion distribution functions presented in Figures 5 and 8, respectively. Note that although Cluster is traveling from left to right with ~3 km/s, the motion of the flux tubes by the spacecraft both naturally and due to variations of P_{dyn} in solar wind is much faster, possibly resulting in observed sequence of events in the time series.
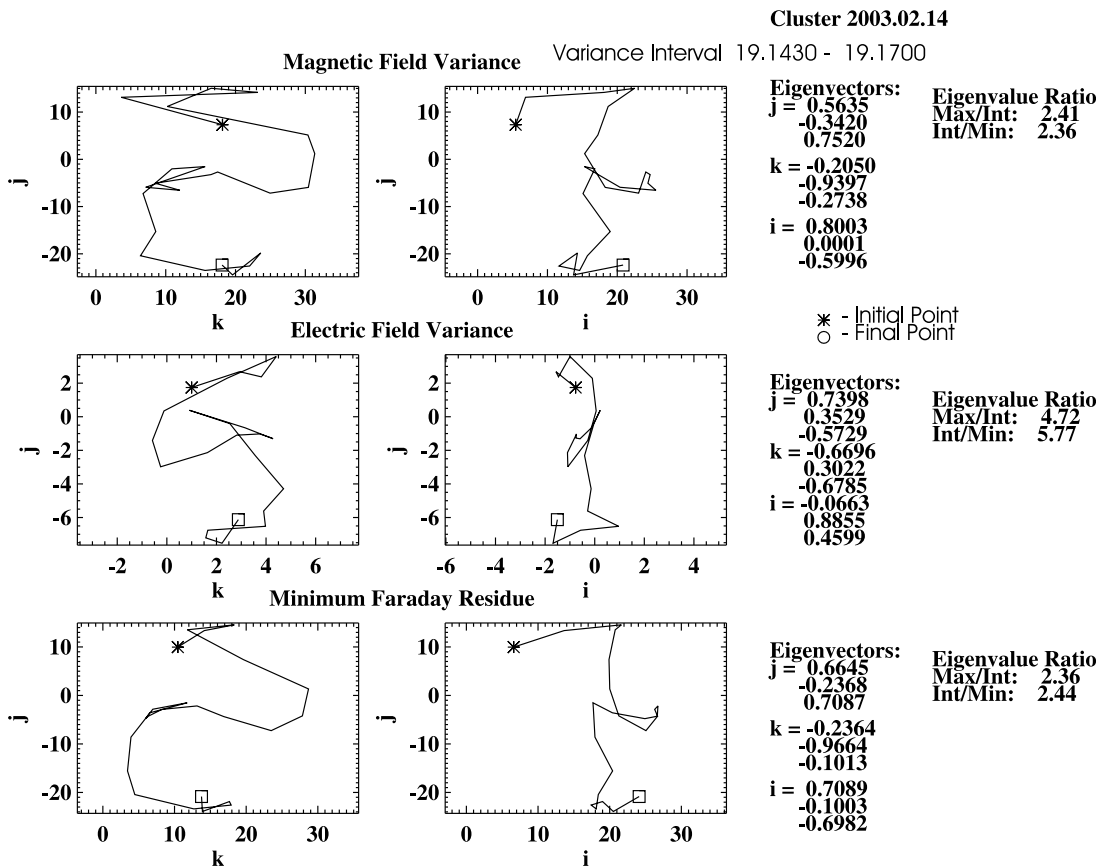
Figure 7. (top) MVAB, (middle) MVAE, and (bottom) MFR hodograms during the extended reconnection interval at 1908:34–1910:12 UT presented in Figure 5.

Table 2. Properties of Reconnection Intervals Between 1925 and 2025 UT

Interval (UT)	Decimal Hour	Sc	Walén Slope	Walén Correlation Coefficient	HT Slope	HT Correlation Coefficient	HT Velocity (km/s)
1925:01–1925:16	19.4170–19.4213	4	0.94	1.00	0.99	0.99	[200, −151, −165]
1925:35–1926:26	19.4264–19.4408	1	1.12	1.00	0.93	0.96	[138, −230, −129]
1928:01–1928:18	19.4672–19.4717	4	0.87	1.00	0.94	0.97	[166, −184, −83]
1928:00–1928:55	19.4669–19.4820	1	0.86	1.00	0.89	0.95	[60, −134, −67]
1930:28–1931:01	19.5079–19.5170	1	0.95	0.97	0.82	0.91	[40, −262, −113]
1940:18–1941:31	19.6719–19.6920	1	0.91	0.99	0.87	0.93	[69, −256, −87]
1941:45–1942:10	19.6961–19.7028	1	0.74	0.99	0.90	0.96	[127, −184, −76]
1950:45–1950:57	19.8461–19.8494	4	1.07	0.99	0.91	0.95	[262, −232, −81]
1950:56–1951:50	19.8490–19.8640	1	1.16	0.97	0.85	0.92	[244, −185, −96]
1951:46–1951:58	19.8630–19.8663	1	0.90	0.99	0.99	1.00	[172, −154, −84]
1952:04–1952:16	19.8680–19.8713	1	1.12	1.00	0.95	0.98	[199, −150, −144]
1952:36–1953:20	19.8767–19.8889	1	0.86	1.00	0.87	0.93	[139, −146, −79]
2000:36–2001:28	20.0100–20.0245	4	0.74	0.92	0.82	0.93	[−116, −83, 76]
2001:19–2001:44	20.0222–20.0289	4	0.79	0.97	0.86	0.93	[−155, −59, 99]
2004:37–2005:06	20.0772–20.0850	1	0.79	0.96	1.00	1.00	[−304, −124, 196]
2005:39–2005:51	20.0942–20.0975	3	−0.87	−0.96	0.95	0.98	[−270, −327, 156]
2006:34–2006:46	20.1097–20.1130	3	0.97	0.91	0.97	0.98	[−203, −33, 391]
2007:39–2007:51	20.1275–20.1311	3	0.87	0.90	0.98	0.99	[−179, −45, 15]
2007:40–2008:12	20.1280–20.1369	1	0.85	0.96	0.91	0.96	[−225, −21, 277]
2007:37–2007:49	20.1270–20.1303	4	0.84	1.00	0.96	0.98	[−386, −60, 185]
2007:40–2007:58	20.1280–20.1330	3	1.00	1.86	0.96	0.98	[−252, −20, 31]
2009:39–2010:12	20.1610–20.1702	1	0.99	0.94	0.97	0.99	[−342, 10, 215]
2010:26–2010:38	20.1740–20.1773	3	0.81	0.96	0.92	0.96	[−129, 15, 144]
2010:33–2011:01	20.1760–20.1838	3	0.79	0.94	0.89	0.94	[−218, 43, 202]
2012:25–2012:37	20.2070–20.2103	1	−1.08	−1.00	0.93	0.96	[−22, 242, −97]
2016:54–2017:34	20.2818–20.2929	3	−0.79	−0.99	0.93	0.97	[−262, 210, 130]
2023:44–2024:12	20.3958–20.4036	1	−0.73	−1.00	0.98	0.99	[−281, 185, 205]

ward IMF. The HT frame velocity of the tailward moving flux tube is [−250, −20, 31] km/s, and compared to previous sc1 interval illustrated in Figure 5 the particle distribution functions show more variability: At the beginning of the interval (Figure 8c) most flux is in the first and fourth quadrant indicating that particles are streaming both parallel and antiparallel to magnetic field; at the center of the interval (Figure 8d) the parallel population becomes more dominant and at the end of the interval ions propagate mostly antiparallel to magnetic field. During this interval the b_x rotates from positive to negative to positive and simultaneously plasma flow speed increases first from ~100 km/s to 325 km/s and then drops back to ~250 km/s. There are also strong variations in other components, but the rotation of b_x gives the clearest signature in order to interpret how sc3 might be moving with respect to the reconnected flux tube. The cartoon in Figure 6b illustrates the relative trajectory of sc3 by the reconnected flux tube in order to explain the observed signature: (1) this field line reconnected first which is indicated by reduced tailward flow, presence of both incoming and reflected ion population (see Figure 8c), positive b_x and negative b_z; (2) this field line reconnected later having larger tailward flow, larger incoming ion population, smaller reflected population, small negative b_x and b_z indicating that sc3 is crossing that close to the middle; and (3) this field line reconnected last which is indicated by tailward flow with positive v_z. Positive b_x, negative b_z, reduced plasma temperature and strong antiparallel population indicate that sc3 crossed this field line into the magnetosheath side. Here also the variable dynamic pressure of the solar wind can result in relative motion of the flux tubes by the spacecraft. The MVAE hodogram (not shown) of the extended interval (2007:40–2008:24 UT) measured by sc3

shows an S-shaped hodogram, similar to sc1 interval in Figure 7, while MVAB and MFR tests show an upper curve of S shape and a squeezed lower arc of the S.

4.3. Abnormalities in Observations of Reconnection Signatures

[34] Most of the reconnection signatures were consistent with expected reconnection geometry during northward and southward IMF with strong b_y but we also encountered some puzzling observations. Sc3 observes a negative slope during southward IMF with strongly enhanced negative v_y component of the HT frame velocity (see sc3 interval in Table 2 at 2005:39–2005:51 UT). Examination of plasma and magnetic field data (not shown) indicates that during this interval plasma density gets reduced from ~10/cc to ~3/cc; b_x changes from ~−30 nT to −18 nT; b_y varies between −30 nT to −20 nT; b_z changes from +19 nT to 5 nT and plasma velocity gets reduced from 330 km/s to 100 km/s. This may suggest that sc3 crossed a reconnected flux tube (type C) more at the magnetospheric side (see cartoon of the magnetic field geometry in Figure 6b, which shows that b_x (b_z) should be negative (positive) on magnetospheric side of reconnected flux tube #3).

[35] The last two intervals with northward IMF showed a strongly positive v_z component of the HT velocity. Considering the spacecraft have moved more sunward it first seems unlikely that they are observing the tailward moving flux tube originating from lobe reconnection at duskside cusp, also the observed v_z components should be smaller. Understanding these last intervals in Table 2 requires further work, but they might be signatures of dayside component merging or merging between IMF and magnetic flux gen-
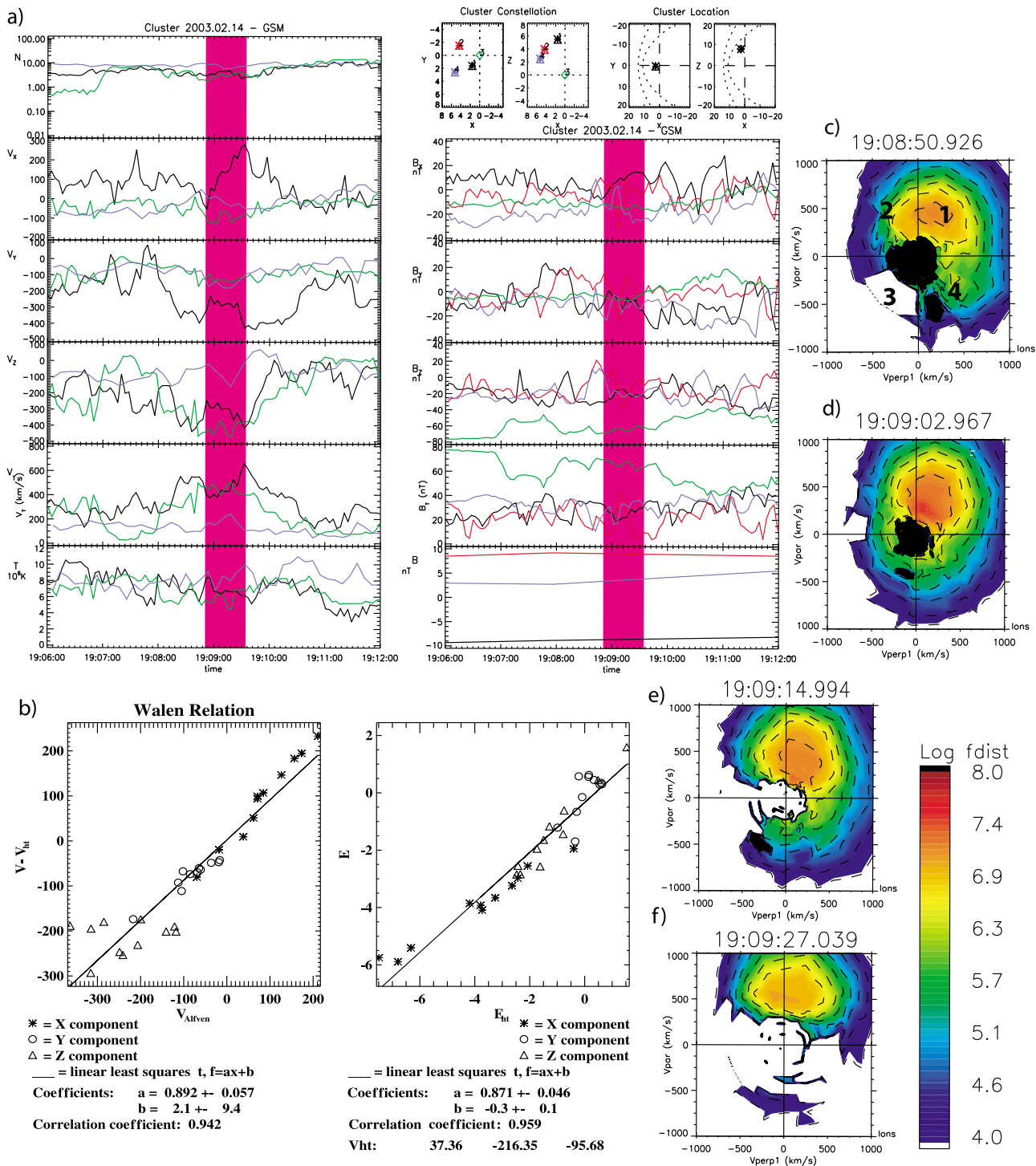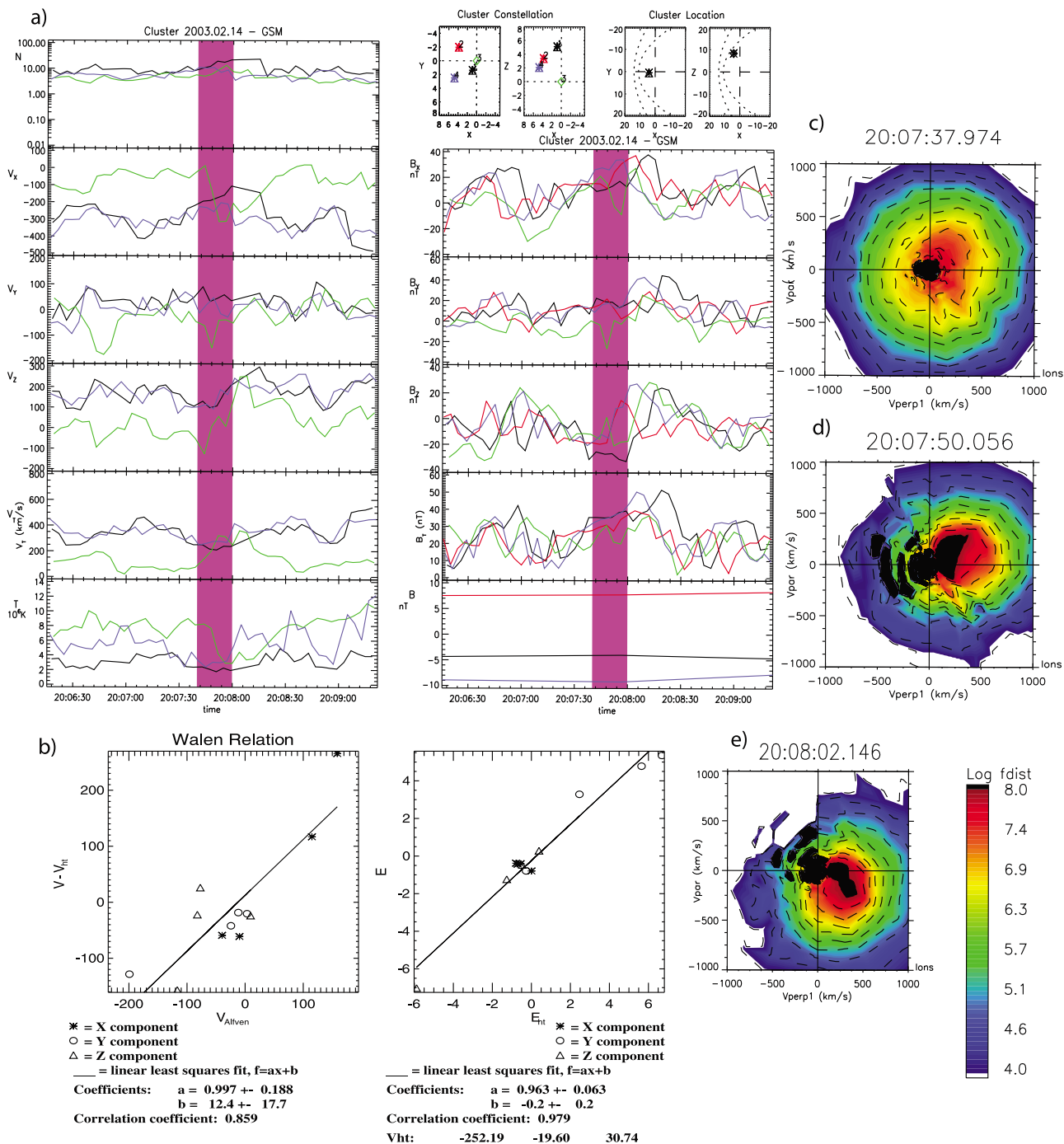
Figure 8. (a) Plots of (left) plasma and (right) magnetic field observations between 2006:15 and 2009:24 UT during southward IMF. (b) Walén relations and HT frames during highlighted interval between 2007:40 and 2008:00 UT measured by sc3. (c–e) Evolution of the ion distribution functions measured by sc3 in the parallel-perpendicular plane between 2007:37 and 2008:02 UT.

erated during previous southward IMF interval. During southward IMF more magnetic flux has piled up at high latitudes (see red field lines in Figure 6b), so when IMF turns northward reconnection occurs between this newly generated (red) flux and IMF resulting in tailward moving flux tubes with positive v_z originating from more dayside (compared to location of the tailward moving flux tube in

Figure 6a) and it would explain why Cluster can observe these closer to dayside.

5. Structure and Size of the Cavity

[36] The size and structure of the DMC is calculated by estimating boundary normal orientations and projecting the

Table 3. Boundary Normals, Average Plateau Eigenvalue Ratios, and Average of Spacecraft Separation Projections Along Plateau Normals Measured by Four Cluster Spacecraft During Boundary Crossings[a]

	Boundary Normals	Eigenvalue Ratios	ΔR_{N14}	ΔR_{N24}	ΔR_{N34}	ΔR_{N12}	ΔR_{N23}	ΔR_{N13}	M Range
Sc1 (Interval 1), MSP-DMC, Reference Interval 1848:00–1851:35 UT, Central Time 1849:47 UT									
Average of plateau MVAB normals	0.99, −0.03, 0.14	$\lambda_2/\lambda_3 = 1.4$	3130	570	5700	2570	5130	2560	no plateau
Average of plateau MVAE normals	0.96, 0.04, 0.28	$\lambda_1/\lambda_2 = 4.7$	2670	600	6080	2070	5490	3420	53–79
Average of plateau MFR normals	0.96, 0.03, 0.27	$\lambda_2/\lambda_3 = 4.1$	2680	560	6050	2110	5470	3380	53–79
Sc4 (Interval 1), MSP-DMC, Reference Interval 1836:00–1853:00 UT, Central Time 1844:30 UT									
Average of plateau MVAB normals	−0.36, 0.91, −0.20	$\lambda_2/\lambda_3 = 2.5$	120	3490	150	3390	3650	260	243–273
Average of plateau MVAE normals	0.95, 0.30, −0.03	$\lambda_1/\lambda_2 = 4.1$	3760	2060	6010	1700	3950	2260	243–273
Average of plateau MFR normals	0.97, 0.26, −0.03	$\lambda_2/\lambda_3 = 2.7$	3650	1920	5990	1830	4070	2240	243–273
Sc2 (Interval 1), MSP-DMC, Reference Interval 1842:00–1850:06 UT, Central Time 1846:02 UT									
Average of plateau MVAB normals	0.79, −0.60, 0.14	$\lambda_2/\lambda_3 = 2.9$	1840	1860	3130	3710	5000	1290	73–83
Average of plateau MVAE normals	no plasma data								
Average of plateau MFR normals	no plasma data								
Sc1 (Interval 1), MSP-DMC, Reference Interval 1855:47–1906:00 UT, Central Time 1900:53 UT									
Average of plateau MVAB normals	0.88, −0.10, 0.46	$\lambda_2/\lambda_3 = 2.8$	1710	290	5680	2010	5980	3970	151–159
Average of plateau MVAE normals	0.87, −0.15, 0.46	$\lambda_1/\lambda_2 = 2.1$	1650	500	5510	2150	6010	3860	149–158
Average of plateau MFR normals	0.88, −0.19, 0.44	$\lambda_2/\lambda_3 = 1.9$	1720	610	5380	2330	5990	3660	149–158
Sc3 (Interval 1), MSP-DMC, Reference Interval 1903:00–1921:00 UT, Central Time 1912:00 UT									
Average of plateau MVAB normals	0.94, 0.16, −0.30	$\lambda_2/\lambda_3 = 4.9$	4520	1950	4680	3710	2740	160	253–281
Average of plateau MVAE normals	0.97, 0.18, −0.15	$\lambda_1/\lambda_2 = 2.9$	4220	1850	5250	2370	3400	1030	253–281
Average of plateau MFR normals	0.96, 0.22, −0.145	$\lambda_2/\lambda_3 = 2.1$	4210	2010	5350	2200	3340	1140	253–281
Sc1 (Interval 2), DMC-MSH, Reference Interval 1917:00–1920:00 UT, Central Time 1918:30 UT									
Average of plateau MVAB normals	0.69, 0.40, 0.60	$\lambda_2/\lambda_3 = 3.3$	1150	1430	6070	290	4640	4930	no plateau
Average of plateau MVAE normals	0.67, 0.43, 0.60	$\lambda_1/\lambda_2 = 6.8$	1110	1560	6060	450	4500	4940	39–45
Average of plateau MFR normals	0.68, 0.47, 0.57	$\lambda_2/\lambda_3 = 3.8$	1290	1780	6100	490	4320	4810	39–45
Sc4 (Interval 2), DMC-MSH, Reference Interval 1917:00–1921:00 UT, Central Time 1919:00 UT									
Average of plateau MVAB normals	0.81, 0.34, 0.46	$\lambda_2/\lambda_3 = 4.3$	2010	1520	6260	500	4740	4240	59–69
Average of plateau MVAE normals	0.67, 0.54, 0.52	$\lambda_1/\lambda_2 = 5.4$	1470	2120	6100	660	3980	4630	59–69
Average of plateau MFR normals	0.62, 0.58, 0.53	$\lambda_2/\lambda_3 = 4.0$	1320	2250	6000	930	3760	4690	59–69
Sc2 (Interval 2), DMC-MSH, Reference Interval 1918:35–1923:24 UT, Central Time 1921:00 UT									
Average of plateau MVAB normals	0.75, 0.21, 0.62	$\lambda_2/\lambda_3 = 3.7$	1150	690	5940	460	5250	4790	61–71
Average of plateau MVAE normals	no plasma data								
Average of plateau MFR normals	no plasma data								
Sc4 (Interval 3), MSH-DMC, Reference Interval 1924:18–1924:50 UT									
Average of plateau MVAB normals	0.40, 0.07, 0.92	$\lambda_2/\lambda_3 = 19.4$	1200	620	4380	590	4990	5580	no plateau
Average of plateau MVAE normals	0.36, −0.03, 0.93	$\lambda_1/\lambda_2 = 21.5$	1480	1120	3970	360	5100	5450	no plateau
Average of plateau MFR normals	0.39, −0.09, 0.92	$\lambda_2/\lambda_3 = 28.2$	1400	1330	3920	70	5250	5320	no plateau
Sc4 (Interval 4), DMC-MSH, Reference Interval 1924:50–1925:12 UT									
Average of plateau MVAB normals	0.23, 0.08, 0.97	$\lambda_2/\lambda_3 = 27$	1990	810	3660	1190	4460	5650	no plateau
Average of plateau MVAE normals	0.15, 0.17, 0.97 (int)	$\lambda_1/\lambda_2 = 1.9$	2200	510	3490	1690	4000	5690	no plateau
Average of plateau MFR normals	0.14, −0.02, 0.99	$\lambda_2/\lambda_3 = 10.7$	2470	1370	2990	1100	4360	5470	no plateau

[a]MSP-DMC, DMC-MSH, and MSH-DMC denote magnetosphere-cavity, cavity-magnetosheath, and magnetosheath-cavity crossings between 1848 and 1926 UT, respectively.

spacecraft separation pairs along these boundary normal directions. We have calculated the normals with three different methods: minimum variance of the magnetic field (MVAB), maximum variance of −**VxB** electric field (MVAE) and minimum Faraday residue method (MFR), except that for sc2 we only use MVAB technique due to lack of plasma data.

[37] We have not used multispacecraft techniques such as Constant Thickness Approach (CTA) [e.g., *Haaland et al.*, 2004] for determining boundary orientation due to following reasons: (1) the spacecraft separation is so large that during the magnetosphere-cavity crossing (≈1840–1900 UT at sc1, sc2 and sc3) sc3 crosses the cavity 30 min later than other spacecraft and at different altitude so there is not good correlation between four spacecraft measurements; (2) IMF conditions have changed during this 30 min interval, so that by the time sc3 gets into the cavity the b_z is dominating over b_y so the reconnection site and thus the boundary normal orientation have possibly changed as sc3 crosses the boundary; and (3) when determining the orientation of the cavity-magnetosheath boundary only three of the spacecraft are doing the transition from cavity to sheath.

[38] Because the normal calculations are sensitive to the fluctuations in the data and length of the analysis window we have checked the time stationarity and error estimates for the normals by doing MVAB, MVAE, MFR on sets of nested data segments centered at the middle (or close to middle) of the current sheet [*Sonnerup and Scheible*, 1998].

Table 4. Boundary Normals, Average Plateau Eigenvalue Ratios, and Average of Spacecraft Separation Projections Along Plateau Normals Measured by Four Cluster Spacecraft During Boundary Crossings[a]

	Boundary Normals	Eigenvalue Ratios	ΔR_{N14}	ΔR_{N24}	ΔR_{N34}	ΔR_{N12}	ΔR_{N23}	ΔR_{N13}	M Range
Sc1 (Interval 5), MSH-DMC-MSH, Reference Interval 1940:28–1942:28 UT, Central Time 1941:28 UT									
Average of plateau MVAB normals									no plateau
Average of plateau MVAE normals	0.53, −0.10, 0.84	$\lambda_1/\lambda_2 = 14.4$	640	1090	4290	450	5370	4920	33–39
Average of plateau MFR normals	0.52, −0.06, 0.85	$\lambda_2/\lambda_3 = 9.6$	660	950	4350	300	5310	5010	33–39
Sc4 (Interval 5), MSH-DMC-MSH, Reference Interval 1940:12–1941:42 UT, Central Time 1940:57 UT									
Average of plateau MVAB normals									no plateau
Average of plateau MVAE normals	0.54, 0.28, 0.79	$\lambda_1/\lambda_2 = 4.8$	60	650	5200	670	4550	5230	23–35
Average of plateau MFR normals	0.55, 0.28, 0.79	$\lambda_2/\lambda_3 = 4.6$	70	640	5230	610	4590	5200	23–35
Sc1 (Interval 6), MSH-DMC, Reference Interval 1942:00–2000:00 UT, Central Time 1951:00 UT									
Average of plateau MVAB normals	0.56, 0.06, 0.83	$\lambda_2/\lambda_3 = 4.4$	310	350	4760	50	5120	5070	251–281
Average of plateau MVAE normals	0.44, −0.10, 0.89	$\lambda_1/\lambda_2 = 13.07$	1120	1240	3920	110	5160	5050	251–281
Average of plateau MFR normals	0.46, −0.05, 0.89	$\lambda_2/\lambda_3 = 8.0$	970	1010	4130	40	5140	5100	251–281
Sc2 (Interval 6), MSH-DMC, Reference Interval 1942:00–2000:00 UT, Central Time 1951:00 UT									
Average of plateau MVAB normals	0.57, 0.00, 0.82	$\lambda_2/\lambda_3 = 3.7$	290	580	4690	290	5270	4970	261–279
Average of plateau MVAE normals	no plasma data								
Average of plateau MFR normals	no plasma data								
Sc4 (Interval 6), MSH-DMC, Reference Interval 1945:00–1959:23 UT, Central Time 1952:12 UT									
Average of plateau MVAB normals	0.31, −0.41, 0.86	$\lambda_2/\lambda_3 = 1.7$	1840	2660	2400	820	5070	4250	218–231
Average of plateau MVAE normals	0.56, 0.07, 0.81	$\lambda_1/\lambda_2 = 12.42$	110	230	4880	120	5100	4990	218–231
Average of plateau MFR normals	0.56, 0.02, 0.83	$\lambda_2/\lambda_3 = 6.5$	340	530	4650	190	5180	4990	218–231
Sc1 (Interval 7), DMC-MSH, Reference Interval 1957:00–2027:00 UT, Central Time 2012:00 UT									
Average of plateau MVAB normals	0.76, −0.025, 0.64	$\lambda_2/\lambda_3 = 6.3$	960	250	5020	1220	5280	4060	451–481
Average of plateau MVAE normals	0.55, −0.10, 0.83	$\lambda_1/\lambda_2 = 3.0$	500	1040	4180	530	5220	4690	451–481
Average of plateau MFR normals	0.74, −0.07, 0.67	$\lambda_2/\lambda_3 = 3.5$	730	530	4830	1260	5360	4100	451–481
Sc2 (Interval 7), DMC-MSH, Reference Interval 1954:00–2027:00 UT, Central Time 2010:30 UT									
Average of plateau MVAB normals	0.70, −0.11, 0.70	$\lambda_2/\lambda_3 = 6.0$	440	780	4650	1220	5440	4220	481–509
Average of plateau MVAE normals	no plasma data								
Average of plateau MFR normals	no plasma data								
Sc3 (Interval 7), DMC-MSH, Reference Interval 1954:00–2030:00 UT, Central Time 2012:00 UT									
Average of plateau MVAB normals	0.50, −0.34, 0.80	$\lambda_2/\lambda_3 = 2.0$	850	2080	3310	1230	5390	4160	501–551
Average of plateau MVAE normals	0.55, −0.07, 0.83	$\lambda_1/\lambda_2 = 5.6$	460	900	4300	440	5200	4760	501–551
Average of plateau MFR normals	0.67, 0.03, 0.72	$\lambda_2/\lambda_3 = 3.2$	530	200	4990	720	5190	4470	501–551
Sc4 (Interval 7), DMC-MSH, Reference Interval 1954:00–2027:00 UT, Central Time 2010:30 UT									
Average of plateau MVAB normals	0.60, −0.22, 0.77	$\lambda_2/\lambda_3 = 7.0$	270	1460	4020	1190	5470	4280	481–521
Average of plateau MVAE normals	0.53, −0.12, 0.84	$\lambda_1/\lambda_2 = 3.9$	650	1180	4080	530	5250	4720	481–521
Average of plateau MFR normals	0.60, −0.13, 0.79	$\lambda_2/\lambda_3 = 3.4$	220	1060	4310	830	5360	4530	481–521

[a]MSH-DMC, MSH-DMC-MSH, and DMC-MSH denote magnetosheath-cavity, magnetosheath-cavity-magnetosheath, and cavity-magnetosheath crossings between 1940 and 2030 UT, respectively.

The smallest segment has only three data points (M value of 3), and then each subsequent segment has one additional data point added at both ends (M value increases by increments of two). Appendix A shows an example of plateau normal calculation with error estimates.

[39] Tables 3 and 4 present the results of the average plateau normals measured by different spacecraft during different current sheet crossings and lists the spacecraft separation vectors (rounded to nearest ten) projected along Average Plateau Normals (APN). The time denotes the reference interval for reference normal (see Appendix A for more details) and approximate central current sheet time at the middle of each nested segment. The M value lists the segment used for plateau normal calculation. If no good plateau normal is obtained the time interval and normal yielding the best eigenvalue ratio is marked. For interval 1924:50–1925:12 UT, the intermediate direction of the MVAE normal is marked because it seems that maximum and intermediate eigenvector of MVAE test had switched places.

5.1. Magnetosphere-Cavity Transition

[40] The first crossing is the magnetosphere-cavity (MSP-DMC) transition that occurs gradually at all spacecraft. For sc1 this transition is from 1848:00–1851:35 UT and both MVAE and MFR yield a stable plateau normal with very similar eigenvectors which have a dominant x component of 0.96. The MVAB test has the smallest eigenvalue ratio but the normal is still not significantly different from those calculated from MVAE and MFR tests: the angle between MVAB normal and MFR normal is ~9°. Sc1 is briefly swept back to the magnetosphere due to pressure increase at ~1853–1855 UT after which it returns back to cavity when dynamic pressure decreases measuring a normal (although still with the largest x component) tilted more toward positive z direction. Sc4 which is at lower altitude and further

duskside observes at 1836–1853 UT also stable MFR and MVAE normals with largest x component (0.95 and 0.97, respectively), but now the normals are tilted more toward positive y direction than measured at sc1 location (the normal from MVAB test has the lowest eigenvalue ratio and yields a completely different normal: the angle between MVAB and MFR normal is ~84°). Sc2 which is furthest dawnward also observes a normal with largest x component but now with a strong tilt toward negative y direction. For sc3 which is at lowest altitude and between sc1 and sc2 in y direction, the transition from MSP to cavity occurs last at 1903–1917 UT and it also observes the largest x component but now the normal is slightly tilted toward positive y and negative z direction. The observations of normals with the largest x component and tilt toward positive (negative) z direction at higher (lower) altitude are consistent with Cluster location with respect to magnetic field line topology from the T89 model (see Figure 13 and discussion on the cavity structure). The differing y components of the normals indicate that magnetosphere-cavity boundary has curvature in x - y plane within spacecraft separation.

[41] By 1915 UT all the spacecraft have moved from magnetosphere into cavity which allows us to calculate the minimum extent of the cavity by choosing the maximum value of projected spacecraft pair distances along various directions. From now on we discuss only the projected distances along the plateau normals (if they exists) obtained with the test that returns best eigenvalue ratios during plateau observations. The maximum extent (width) along sc3 normal vector [0.94, 0.16, −0.30] (sc3 and sc4 separation projected along this normal) is 4680 km and 6090 km along sc1 normal vector (see Table 3). The projection of sc4 and sc3 separation vector along z direction of the cavity at 1915 UT is 5440 km. The extent along x direction (projection of sc4 and sc3 separation vectors along x direction) is 5230 km and along y direction 4170 km which is measured between sc2 and sc4. The actual extent of the cavity may be even larger than this as sc1 and sc4 move from cavity into magnetosheath at ~1917 UT due to enhanced dynamic pressure (see Figure 2k). Although the dynamic pressure shows lots of variations, the average pressure is much higher during the magnetosheath interval compared to cavity interval.

5.2. First Cavity-Magnetosheath Transition

[42] Velocity and magnetic field data indicate that the transition from diamagnetic cavity to the magnetosheath occurs almost simultaneously for sc1 and sc4, except that for sc1 the gradients are slightly sharper. However, the temperature data shows that sc1 leads sc4 by 1 min in the transition. Table 1 indicates that for sc1 this transition satisfies the reconnection criteria, suggesting that diamagnetic cavity-magnetosheath (DMC-MSH) boundary is a rotational discontinuity. The orientation of this DMC-MSH boundary is tilted more toward positive z direction compared to MSP-DMC boundary. The MVAE test returns eigenvectors with the best eigenvalue ratios for plateau normals.

The normals that sc1 and sc4 measure are very similar: [0.67, 0.43, 0.60] for sc1 and [0.67, 0.54, 0.52] for sc4. Examination of Cluster constellation in Figure 1 indicates that sc1 and sc4 separation vector is almost perpendicular to these normals in $x − z$ plane, which at first would seem to explain why an increased dynamic pressure would move the DMC-MSH boundary over these spacecraft nearly simultaneously. However, sc2 is much closer to sc1 and sc4 along these boundary normals compared to mutual separation between sc1 and sc4, so it is surprising that it enters to the magnetosheath about 3 min later than sc4. This can be either if the cavity-magnetosheath boundary is further outward at the location of sc2 or the cavity boundary moves toward negative y direction instead of purely along boundary normal direction. The strong peak at solar wind dynamic pressure coincides with sc2 transition into the magnetosheath which may explain the sideways motion of the cavity boundary. Sc3 remains in the cavity during the entire cavity interval which allows us to calculate the minimum extent of the cavity along the boundary normals measured by sc1, sc2 and sc4. These depths are 6060, 5940 and 6100 km for sc1, sc2 and sc4, respectively. However, it is unclear how far below sc3 the cavity actually extends.

5.3. Observations of Cavity-Like Plasma During Magnetosheath Intervals

[43] During the magnetosheath interval at ~1917–1952 UT, spacecraft have brief encounters with the cavity-like plasma. At 1924:18–1925:12 UT as the dynamic pressure drops from a peak value measured at ~1922:00 UT, the magnetopause moves outward and sc4 drops briefly back into cavity-like plasma characterized by depressed field, increased plasma temperature of 10–11 MK and departure from magnetosheath-like flow. RAPID data in Figure 4 show significant fluxes of ~200 keV electrons, ~300 keV protons and ~400 keV Helium (we cannot say whether this is Helium+ or Helium ++) during this interval. See Nykyri et al. (submitted manuscript, 2010) for detailed analysis of high-energy particle observations. Tables 1 and 2 indicate that parts of this interval satisfy the reconnection criteria for sc4 indicating that this signature is a rotational discontinuity.

[44] The magenta colored column in Figure 9a shows plasma and magnetic field measurements, and Figure 9b shows hodograms during 1924:18–1925:16 UT during sc4 encounter with cavity-like plasma. The de Hoffman–Teller frame velocities measured by sc4 at 1924:16–1924:29 UT and 1925:01–1925:16 UT are [213, −112, −55] km/s and [200, −151, −165] km/s, respectively, which are consistent with flux tubes moving sunward (toward positive x), earthward (decreasing z) and dawnward (toward negative y) from reconnection site at the duskside of the cusp. We have compared the plasma and magnetic field observations by sc4 with 2.5-D MHD simulations of the FTE. The simulation code and application for dayside reconnection is explained by Nykyri et al. [2003b] and Otto [1995] and here it is run for the magnetic field and plasma parameters observed

Figure 9. (a) Plasma and magnetic field observations and (b) hodograms during cavity interval measured by sc4 between 1924:18 and 1925:16 UT. The Walén relations and HT frames are satisfied at both edges of depressed B field signature (c) at 1924:16–1924:29 UT and (d) at 1925:01–1925:16 UT but not during the entire interval at 1924:18–1925:16 UT (not shown).
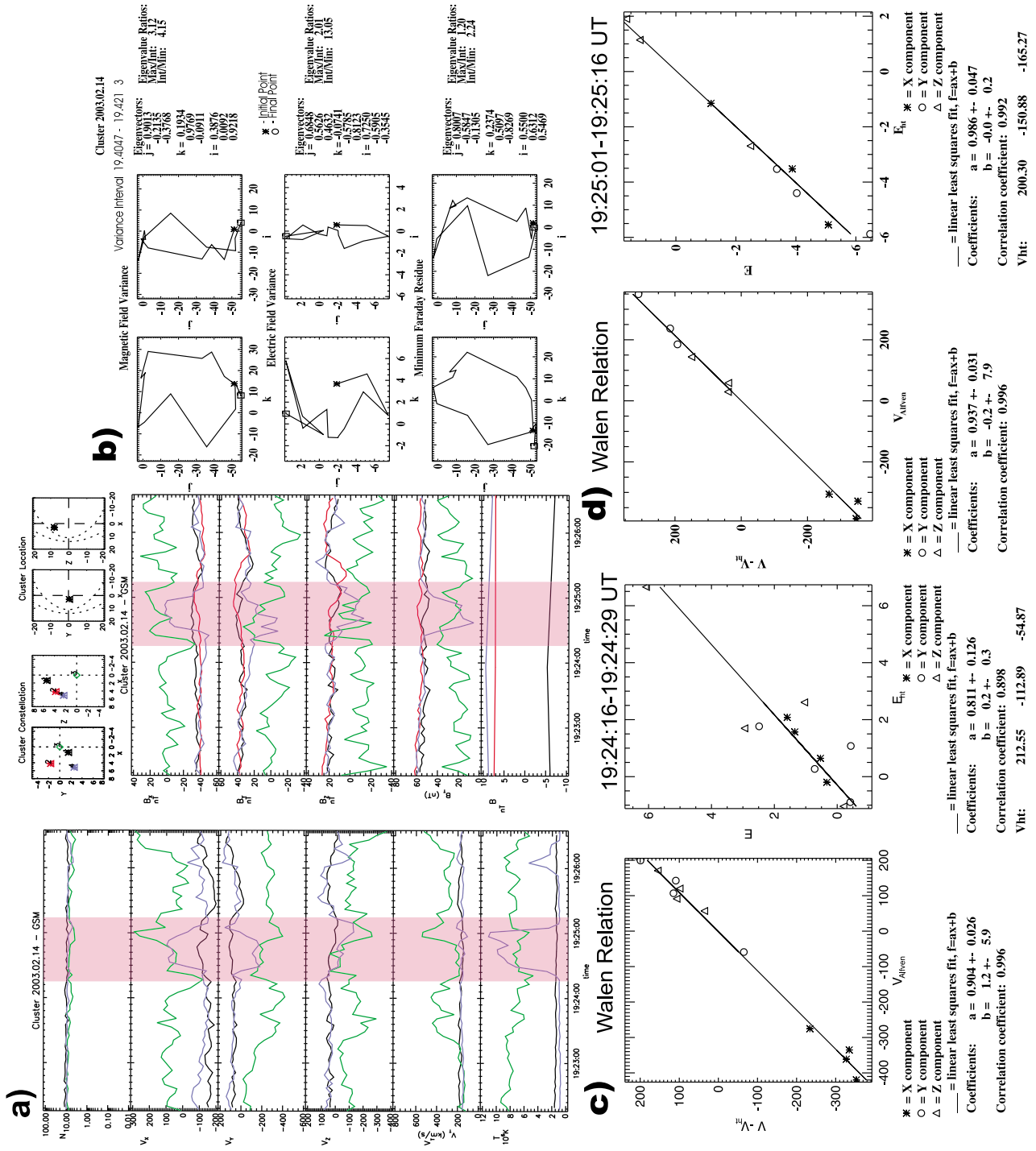
Figure 9

during magnetosheath/cavity crossing in high-altitude cusp: number density is normalized to $10/cm^3$, magnetic field, B_0 is 50 nT, Alfvén speed is 345 km/s, length scale, L_0, is 400 km and time unit, t_0 is 1.16 s. The density is higher on magnetosheath side and magnetic field is larger on magnetospheric side. Figures 10a and 10b show simulation results (see caption of Figure 10 for more details) at t = 159.96 t_0 and at t = 219.97 t_0 together with the cartoon in Figure 10c depicting the FTE geometry together with sc4 trajectory relative to FTE structure.

[45] The normal component of magnetic field and plasma velocity in Figures 10a and 10b is the x component in simulation units and the FTE is propagating toward positive z direction. The x coordinate of the simulation box corresponds roughly to z_{GSM}, the z coordinate of the simulation box corresponds roughly to direction of the de Hoffman–Teller frame velocity which is mostly into direction of x_{GSM} and $-y_{GSM}$, the y coordinate of the simulation box goes into the paper (right-handed coordinate system) and points roughly out of the FTE cartoon (Figure 10c) tilted more toward y_{GSM}. The simulation indicates that the reconnection flow is stronger on the magnetospheric side of the reconnected field line consistent with Cluster observations and that magnetic field is rather weak inside the FTE (green bubble). This region of depressed field essentially is the diamagnetic cavity.

[46] The MVAB analysis (Figure 9b) gives the best eigenvalue ratio for the interval 1924:18–1925:16 UT and shows a clearly polarized ellipse in maximum intermediate plane. The normal is [0.38, 0.0, 0.92] so it is mostly along positive z_{GSM} direction tilted slightly toward positive x_{GSM}, which corresponds to x component in simulation coordinates. Projecting the average magnetosheath magnetic field, [−40.16, 34.55, 20.25] nT measured by sc4 between 1922 and 1924 UT along the boundary normal direction yields a normal component of 3.42 nT. A cut along the x direction at $z = 25$ in Figure 10b (mimicking sc4 trajectory over this structure (see yellow path in Figure 10c)) shows first a normal component that is closely zero but then it becomes negative inside the FTE. Rotating Cluster data into boundary normal coordinates shows that inside FTE the normal component becomes negative reaching the maximum value of −14 nT. Also the magnetic field along the intermediate variance direction which is mostly along y direction changes from positive to negative. This corresponds to the color coded out of the plane magnetic field component (b_y) in Figure 10 which shows that it also changes from positive to negative as one crosses from magnetosheath into the FTE (the color code changes from negative to positive because positive y points into the paper). These observations are in excellent agreement with the simulations of a FTE which support our hypothesis that sc4 indeed crosses into diamagnetic cavity bounded by the FTE structure between 1924:18–1925:16 UT. Note that during the entire sheath interval sc3 remains in the cavity and observes similar plasma and magnetic field characteristics during part of the FTE interval as sc4. The sc3 separation from sc4 projected along boundary normals (for the tests yielding the best eigenvalue ratios) measured by sc4 at the inbound and outbound transition of this FTE (see Table 3) varies between 3660–3920 km which indicates that cavity may be extending at least 3660 km below sc4 along boundary normal

direction. The separation between sc3 and sc4 along normal, [0.38, 0.0, 0.92], measured during the entire FTE interval is even larger, 4180 km. The separation between sc4 and sc3 during this interval is 6220 km.

[47] An immediate question is if this FTE is releasing hot magnetospheric or magnetosheath plasma into cavity or does the FTE open up the cavity and let cavity-like plasma escape antiparallel to magnetic field. The ion distribution functions are presented in Figure 11, and Figure 10c shows a cartoon depicting the FTE geometry together with letters a–g marking the intervals when the distribution functions were observed relative to FTE structure along sc4 trajectory. In the following we will describe the magnetic field and plasma observations along sc4 orbit at points a–g and utilizing information presented in Figures 9–11.

[48] 1. At 1924:04 UT (point a; see Figure 11a) sc4 is in the magnetosheath field line that has not yet reconnected and has negative b_x, positive b_y and b_z, and a magnetosheath-like flow of ∼−200 km/s. The ion distribution function is showing in addition to the typical D-shaped magnetosheath population a higher-energy population at very oblique and perpendicular pitch angles, some of which are propagating antiparallel to the magnetic field. These high-energy particles with velocities of ∼1000 km/s could either be particles that are trapped in the cavity but are observed in the limited region in the magnetosheath due to their larger gyroradius or they could be particles of bow shock origin. Indeed it has been shown that quasi-parallel bow shock maps to the cusp during this event (K. Trattner et al., Cluster observations of bow shock energetic ion transport through the magnetosheath into the cusp, submitted to *Journal of Geophysical Research*, 2010). The gyroradius of the proton that is trapped in the cavity at 10 nT field and has perpendicular velocity of 1000 km/s is 1044 km, so it is quite possible that these trapped cavity particles are observed in the limited region at the magnetosheath up to 1000 km from cavity boundary.

[49] If indeed sc4 is on the field line that has not yet reconnected, the positive parallel distribution at higher energies could be of bow shock origin. However, bow shock source would not explain the high-energy, antiparallel population.

[50] 2. At 1924:15 UT (point b; see Figure 11b) sc4 is closer to the cavity boundary on magnetosheath (MSH) field line and shows a more pronounced butterfly shape of the distribution.

[51] 3. At 1924:27 UT (point c; see Figure 11c) sc4 encounters the field line at the outer edge of the DMC: magnetic field starts to rotate, plasma temperature starts to increase and the distribution shows a large quantity of particles up to 1000 km/s streaming also antiparallel to magnetic field. The high-energy proton fluxes are larger and there is a significant increase in perpendicular energy.

[52] 4. By 1924:39 UT (point d; see Figure 11d) sc4 moves deeper into DMC and observes a more symmetric distribution function with enhanced high-energy fluxes. The magnetic field becomes more distorted from magnetosheath values and is close to its minimum value observed at 1924:36 UT. The proton gyroradius in this weak field region is larger than the gradient of the boundary which is calculated to be 810–1330 km (separation between sc2 and sc4 along boundary normal directions calculated during the crossing of the FTE structure, see Table 3). The protons
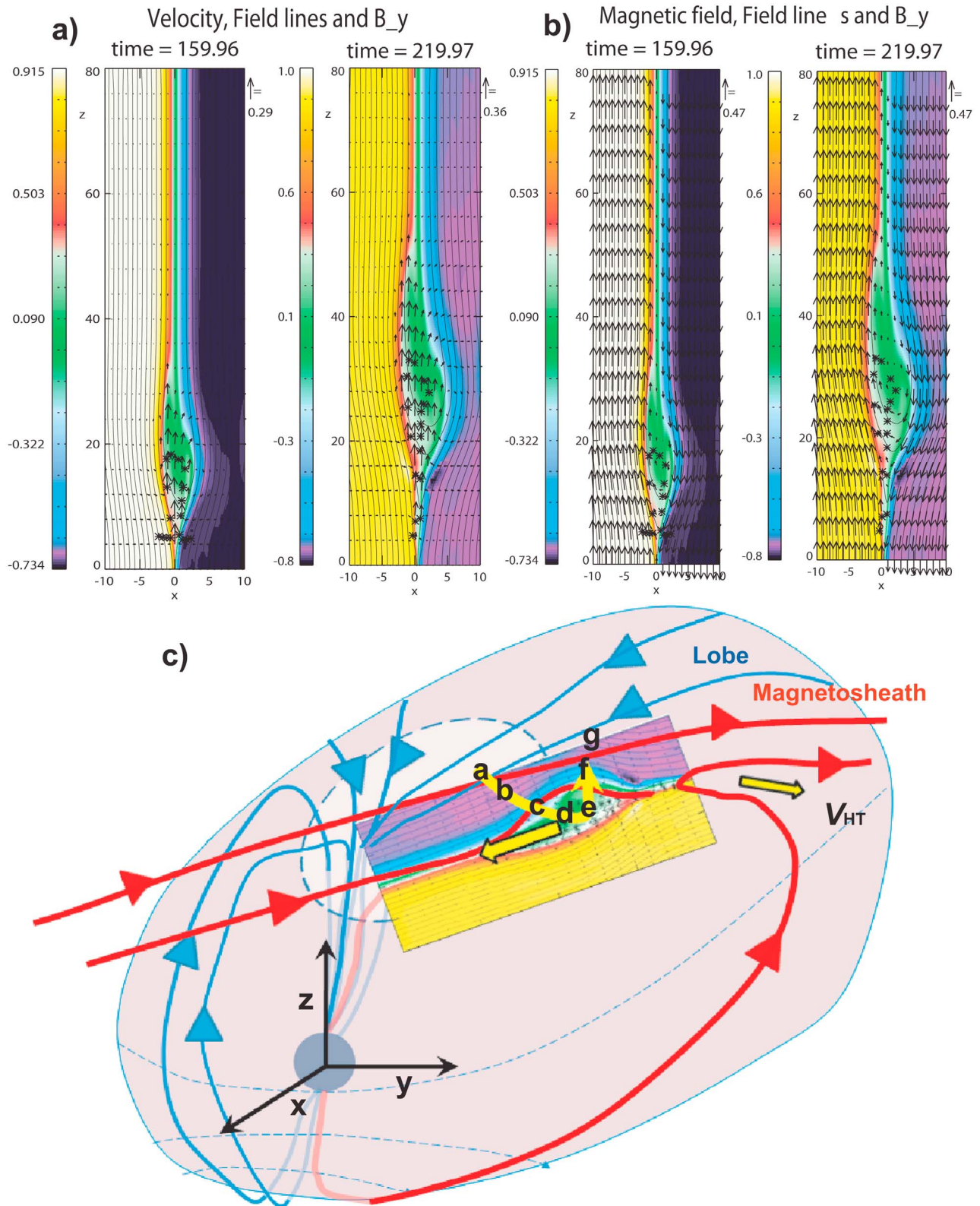
Figure 10. A 2-D MHD simulation of the flux transfer event originating from duskside of the cusp. (a) Time evolution of velocity field vectors and magnetic field lines and (b) magnetic field vectors and magnetic field lines. The background color in both plots depicts the into-the-plane magnetic field component. (c) A 3-D cartoon of the reconnection geometry. The relative trajectory of Cluster sc4 with respect to FTE is plotted with a yellow curve together with letters a–g illustrating times when ion distribution functions shown in Figure 11 are observed.
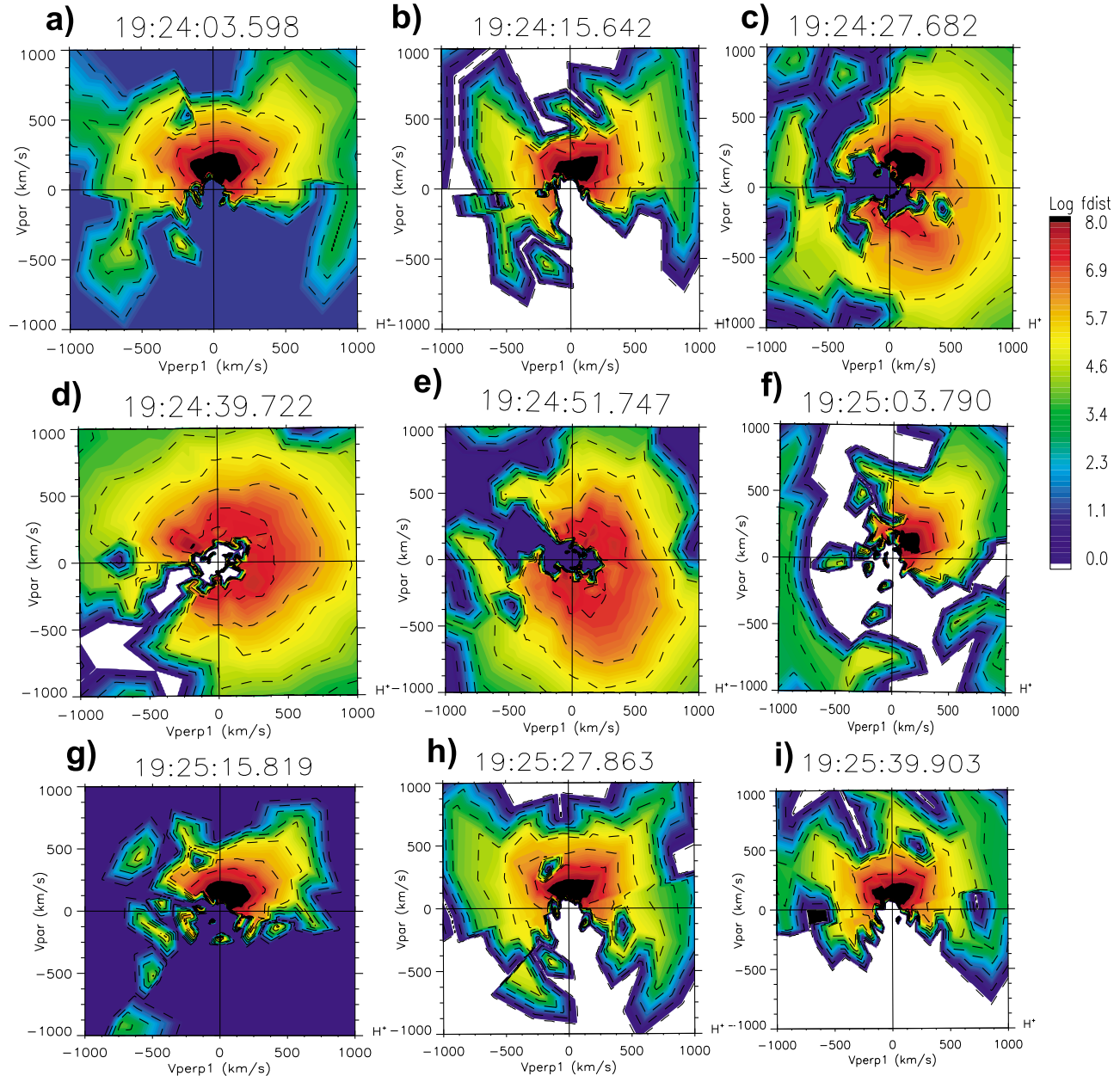
Figure 11. Ion distribution functions measured by sc4 before, after, and during the DMC interval between 1924:18 and 1925:16 UT.

become strongly nonadiabatic and can be pitch angle scattered into the loss cone. This is qualitatively consistent with the observed distribution function which shows that the loss cone is filled, which enables cavity particles to leak into magnetosheath or ionosphere. However, because the magnetic field in the cavity is much weaker than in the magnetosphere or magnetosheath, the loss cone is small. Particles with oblique pitch angles are outside the loss cone and are trapped.

[53] Applying the conservation of the first adiabatic invariant for electrons, shows that the loss cone into the magnetosheath or magnetosphere is extremely narrow and the electron pitch angle distributions show that the majority of the

electrons are trapped (Nykyri et al., submitted manuscript, 2010).

[54] 5. At 1924:51 UT (point e; see Figure 11e) sc4 is still inside DMC and observes higher fluxes of more energetic particles streaming antiparallel than parallel to magnetic field. The loss cone is still filled.

[55] 6. At 1925:03 (point f; see Figure 11f) sc4 is close to DMC-MSH boundary and observes the more typical magnetosheath distribution but also more higher-energy particles at oblique pitch angles and energetic beam propagating antiparallel to this field.

[56] 7. At 1925:15 (point g; see Figure 11g) sc4 has moved into magnetosheath and observes a magnetosheath-
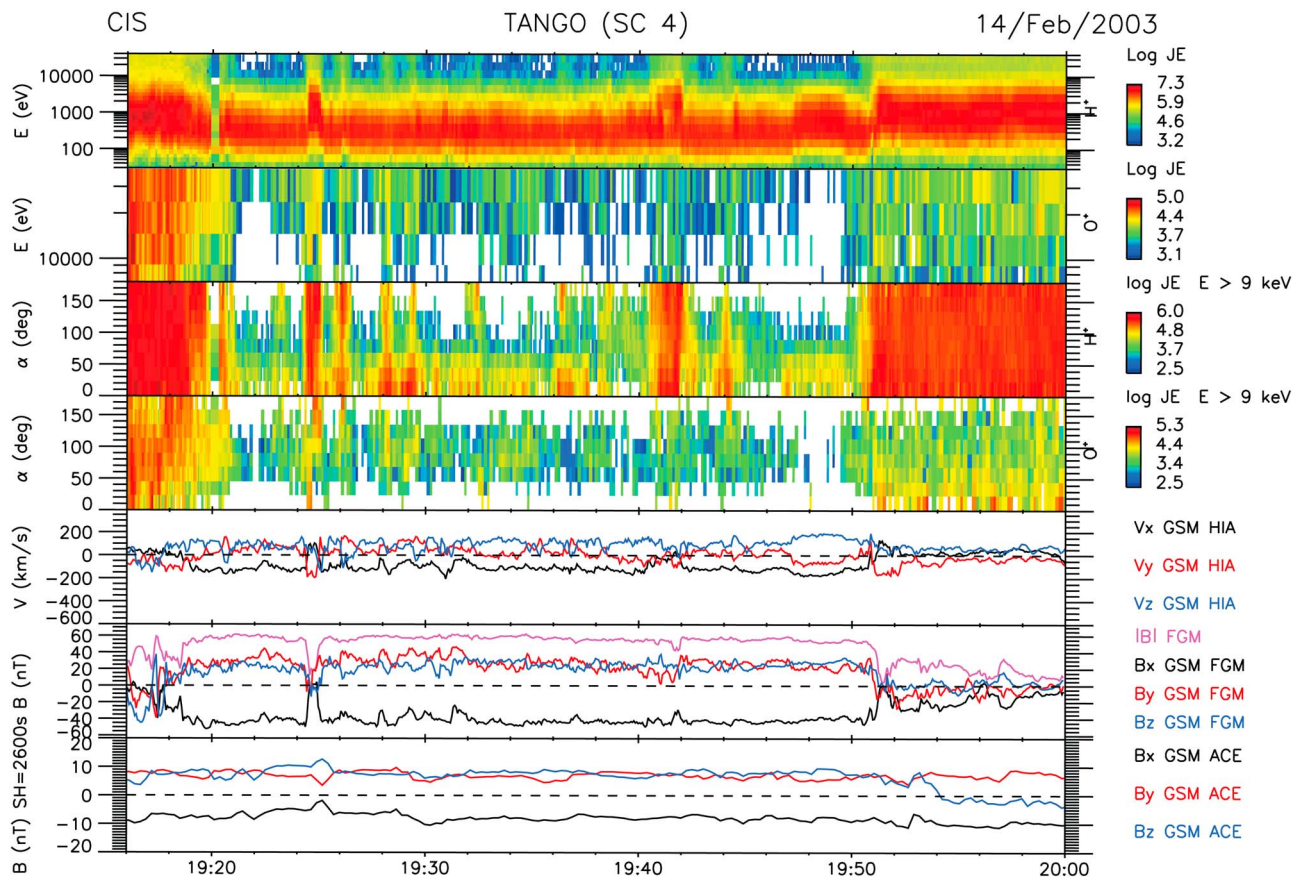
Figure 12. Sc4 observations at 1908–2000 UT during and surrounding the magnetosheath. Shown are proton energy (first panel), O+ energy (second panel), proton pitch angles (third panel), O+ pitch angles (fourth panel), velocity vector (fifth panel), magnetic field (sixth panel), and IMF (seventh panel).

like distribution but still some fluxes antiparallel to magnetic field.

[57] 8. At 1925:28 UT (Figure 11h) and 1925:39 UT (Figure 11i) sc4 has moved closer to the DMC-MSH boundary due to decrease in dynamic pressure of solar wind so the distributions show more higher-energy particles similar to those observed at points a and b.

[58] Figure 12 shows a summary of these sheath interval observations measured by sc4 (see caption for more details). Proton pitch angles vary from 0° to 180° showing clearly more fluxes antiparallel to magnetic field at 1924:18–1925:16 UT which is the first sheath interval exhibiting the FTE signature. In addition this interval shows enhanced fluxes of 10–20 keV O+ ions at 0°–90° pitch angles at the beginning of the interval (corresponding to locations c and d in Figure 10) and 10–40 keV fluxes at 90°–180° pitch angles during the exit from the cavity (corresponding to locations e and f in Figure 10).

[59] O+ could come from magnetosphere into the cavity but because during the beginning of interval the sc4 is on field lines c and d in Figure 10, the population of magnetospheric origin should propagate antiparallel to magnetic field, not parallel. The fact that this is not observed indicates that O+ could originate from DMC. Indeed, during the rest of the magnetosheath crossing, most 30–40 keV O+ is at

60°–120° pitch angles, which would be consistent with leakage from DMC due to large gyroradius of energetic O+.

[60] For the interval corresponding to field lines e and f sc4 observes a trapped population and particles propagating antiparallel to magnetic field which could be of cavity or magnetospheric origin. Note that the O+ fluxes at ~180° pitch angles at 1924:51–1925:04 UT are larger and at higher energies than at other pitch angles and also coexist with the maximum antiparallel proton fluxes. This signature indicates that the source region for O+ and H+ fluxes during this interval may be the same and based on lack of antiparallel O+ fluxes during the beginning of the interval the most likely source is the DMC. *Chang et al.* [2000] showed that there are two types of energetic ions observed in the magnetosheath, one type for H+, He++, and O$^{>2+}$ and the other for He+. Based on spectral properties they suggested that the acceleration region for He+ ions is different from the one(s) for He++, and O$^{>2+}$ ions that were of solar wind origin. Unfortunately the RAPID instrument cannot distinguish the charge state of the observed He ions, so we cannot say whether the observed He ions were of solar wind or ionospheric origin. However, the singly ionized energetic O+ ions have been observed in the DMCs before and they are thought to be of ionospheric origin [*Chen and Fritz*, 2001].

[61] For protons the pitch angle scattering fills the loss cone on a time scale that is faster than the time scale one would see the loss cone emptied. On the other hand, the pitch angle scattering for oxygen within one gyroperiod can get O+ either parallel or antiparallel to magnetic field and can be either swept into ionosphere or lost into magnetosheath. These asymmetric O+ distributions are also observed during other DMC intervals which may suggest that O+ can be energized in the DMC and portion of the distribution can be lost either into the ionosphere or magnetosheath via pitch angle scattering.

[62] We think that the highly oblique and perpendicular high-energy populations that are observed at the boundaries at the DMC could be either the high-energy particles trapped in the cavity but that are observed due to their higher gyroradius at the cavity boundary or they could originate from the bow shock. The large fluxes of ions streaming antiparallel to the magnetic field at 1924:27 UT are ions escaping the DMC: they appear only 12 s after the observations of streaming in distribution on the field line that is just about to reconnect and the counter streaming population is immediately present when the field line is opened. A particle with 500 km/s travels 6000 km in 12 s, so it is unlikely that these could be particles that enter the cavity from the magnetosheath, propagate to mirror point and reflect back. If this was the case, the mirror point should be only 3000 km below sc4. Considering the z coordinate for sc4 is ~53000 km this is very unlikely. We also showed that sc3 has remained in the cavity during the entire sheath interval so the cavity with hot plasma extends likely at least 3660 km along boundary normal direction and 6220 km from sc4 toward sc3, so the cavity is the closest reservoir to explain the immediate presence of these antiparallel particles.

[63] Also during remaining of the magnetosheath interval sc4 remains close to the cavity boundary: it continues to measure lower v_x compared to sc1 that is at higher z coordinate than sc4. Note that as sc4 travels at the vicinity of the DMC boundary in the magnetosheath, it continues to observe the 20–40 keV oxygen ions at very oblique pitch angles. This further supports the idea that oxygen ions of cavity origin are observed in the magnetosheath due to their large gyroradius.

[64] Sc4 has another encounter of hotter cavity-like plasma with reduced v_x and b_t between 1940:24–1942:03 UT and sc1 observes this region of hotter plasma at 1941:42–1942:30 UT. Any parts of this sc4 interval are not picked up by the automated search for reconnection intervals. The Walén relation and HT frames are poorly satisfied at both edges of this structure for sc4, which may indicate that sc4 is not fully crossing the reconnected field line. However, throughout this interval sc4 is measuring ion distribution functions (not shown) similar to Figures 11c and 11e which indicates that it might be observing particles on field line that reconnected recently in the past and therefore shows both parallel and antiparallel population. Interestingly, the antiparallel population is at higher energies than the parallel population (D shape is larger at quadrants 3 and 4 compared to quadrants 1 and 2). For sc1 the Walén relation and HT frame velocity are well satisfied at the inbound edge of this structure at 1941:45–1942:10 UT (see Table 2) and it observes a distribution function where the parallel population is dominating but the antiparallel population at higher

energy is immediately present at 1941:53 UT and gets stronger at the center of this interval. The boundary normals measured by sc1 and sc4 during these intervals (see Table 4) are now tilted more toward x direction compared to previous sheath interval. Sc3 that remains in the cavity during the sheath interval is located 4290–5230 km (4920–5230 km) below sc4 (sc1) along the boundary normal directions measured by sc4 (sc1). Note that now the sc1 rather than sc2 is closer to sc4 along these boundary normal directions measured by sc1 and sc4. The high-energy particles signatures during these sheath intervals are discussed elsewhere (Nykyri et al., submitted manuscript, 2010).

5.4. Magnetosheath-Cavity Transition

[65] Figure 2 shows that as the dynamic pressure of the SW drops by 30%, all spacecraft that were in the magnetosheath are swept back into cavity at ~1952 UT. Note that the IMF is rotating from northward to southward so the reconnection site moves to the sunward side of the duskside cusp and the region of depressed field forms now more sunward compared to the first cavity interval. At the magnetosheath cavity boundary there is a FTE signature observed by sc1, sc2 and sc4. The orientation of the boundary normal measured during the longer interval at ~1945:00–2000 UT from the magnetosheath into the second cavity interval is quite similar (except for one test with poor eigenvalue ratio) at sc1, sc2 and sc4 (interval 6 in Table 4) and also similar to the orientation of the boundary during the second sheath interval (interval 5 in Table 4). For example, sc4 measures a MVAE normal of [0.56, 0.07, 0.81] and sc2 a MVAB normal of [0.57, 0.00, 0.80]. We chose this longer interval for boundary normal determination as the FTE would cause a stronger perturbation to the normal if the interval was shorter. This FTE signature is discussed in detail by *Nykyri et al.* [2011].

5.5. Cavity-Magnetosheath Transition

[66] After 2000 UT the dynamic pressure starts to increase and finally after few oscillations as it reaches the peak value of 4.4 nPa at 2015 UT, all spacecraft move back to the magnetosheath. This final transition into magnetosheath shows more variability in boundary structure within Cluster separation. Sc1 and sc2 measure similar normals (for the tests with best eigenvalue ratios) that are tilted more toward x direction compared to the previous interval: for example, the normal measured by sc2 is [0.70, −0.11, 0.70]. Sc3 and sc4 that are below sc1 and sc2 along the z direction measure higher z components of the normals. For example, sc4 MVAB normal is [0.60, −0.22, 0.77]. When the dynamic pressure reduces again after 2015 UT sc4 briefly drops back into the region of more depressed field. At first it may seem surprising that as the dynamic pressure reaches the bottom value of ~3 nPa at ~2025 UT none of the spacecraft are swept back into cavity. This is because now the IMF has returned back northward so the reconnection site is moved back tailward of the duskside cusp (see Figure 3 for the motion of the diamagnetic cavity with respect to IMF orientation), so the DMC is expected more tailward.

5.6. Summary of the Large-Scale Cavity Structure

[67] Summary of the boundary normal analysis is shown in Figure 13 (see Figure 13 caption for more details). The
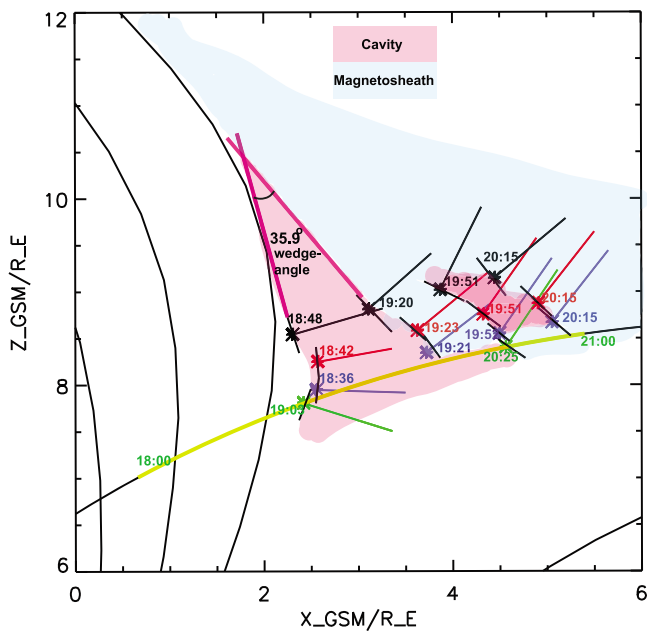
Figure 13. Cavity structure determined from Cluster boundary normal analysis in the *xz* plane superposed on the T89 model. Boundary normals from Tables 3 and 4 are plotted along sc1 (black), sc2 (red), and sc4 (blue) orbits at times corresponding to (1) magnetosphere-cavity, (2) DMC-magnetosheath, (3) magnetosheath-cavity, and (4) DMC-magnetosheath crossings. For sc3 only crossings 1 and 4 are marked as it remains in the cavity up to ~2025 UT. The angle between sc1 normals for crossings 1 and 2 is 35.9° and is denoted as the wedge angle. The thick yellow line shows the sc3 trajectory between 1800 and 2100 UT. Approximate cavity and magnetosheath areas are shaded with light magenta and light blue, respectively.

normals for MSP-DMC transition are plotted at each spacecraft location corresponding to the time at the beginning of the data interval used for normal determination. For example, the first transition for sc1 occurs between 1848 and 1851:35 UT, so we have plotted the normal in *xz* plane at 1848 UT along sc1 trajectory. Normals for DMC-MSH transition are plotted at each spacecraft location at the end of each crossing, normals for MSH-DMC transition are plotted at the center of the each crossing and the normals for the last DMC-MSH transition are plotted ~10 min before the end of the analysis interval because the end of the interval is already quite far in the magnetosheath. We chose to plot the normals at these times because the interval lengths for normal determination using the stability analysis are different for each crossing and sometimes the central time of the interval is far off from the time when spacecraft actually enter (leave) a new (the old) region.

[68] In addition to boundary normals we have plotted short black lines perpendicular to each normal in order to better visualize the boundary structure. The curvature of the magnetosphere cavity boundary agrees quite nicely with the field line curvature from T89 model. The angle between sc1 MSP-DMC and DMC-MSH normals is 35.9° and is denoted as the wedge angle. Sc1, sc2 and sc4 travel to the magne-

toesheath ~1921 UT and when IMF starts turning southward ~1952 UT sc1, sc2 and sc4 reencounter the cavity more sunward. Note that sc3 remains in the cavity the entire time indicating that the new cavity must overlap with the old one. By 2025 UT all spacecraft get into magnetosheath. Note that Figure 13 illustrates the cavity structure only in *xz* plane. Tables 3 and 4 indicate that boundary normals for these crossings can have sometimes significant *y* components.

6. Conclusions and Discussion

[69] In the present study we have analyzed Cluster spacecraft data during a diamagnetic cavity (DMC) crossing at the northern high-altitude cusp characterized by depressed magnetic field and magnetic field fluctuations. The diamagnetic cavity is a highly dynamic region and its location is dependent on the IMF orientation and dynamic pressure. In this section we conclude the main findings of the study and discuss the viability of different sources for high-energy particles.

[70] 1. We have demonstrated that as the IMF changes from northward to southward, the diamagnetic cavity re-forms more sunward. We found fluid and particle evidence of magnetic reconnection that showed flux tubes moving tailward during southward IMF and sunward during northward IMF. Most of the reconnection signatures were consistent with lobe reconnection and subsolar reconnection, but also some puzzling intervals with negative slopes were found (see section 4.3).

[71] 2. The orientations of the boundary normals measured by Cluster are tilted mostly sunward for magnetosphere-cavity (MSP-DMC) boundary and get tilted more toward *z* direction for cavity-magnetosheath (DMC-MSH) boundary.

[72] 3. The extent of the cavity along the MSP-DMC normal direction at sc3 is at least 4680 km and 6090 km at sc1. The extent of the first cavity along DMC-MSH normal at sc4 location is at least 6100 km.

[73] 4. The cavity is filled with high-energy electrons, protons and oxygen ions and high-energy particle fluxes drop several orders of magnitude as spacecraft cross into the magnetosheath.

[74] 5. At the magnetosheath the ion distribution functions show a typical magnetosheath population with no high-energy particles but closer to the DMC boundary a higher-energy population at very oblique pitch angles becomes present.

[75] 6. Throughout the magnetosheath, the high-energy proton fluxes remained low except during brief intervals when sc4 and sc1 dropped back into cavity due to changes in solar wind dynamic pressure. However, the high-energy O+ fluxes did not drop as much in the magnetosheath as the proton fluxes and were mostly at 60°–120° pitch angles, consistent with leakage from DMC due to large gyroradius of the oxygen ions.

[76] 7. Comparison between sc4 data during the brief cavity encounter at 1924 UT and 2.5 D MHD simulations indicates that this interval exhibits a FTE structure. RAPID data shows that this FTE is filled with high-energy electrons, protons and helium and CODIF data showed that in addition to H+ also O+ ions at higher energy are present. Inside the FTE significant fluxes of energized protons and oxygen ions were propagating antiparallel to the magnetic

field, and the antiparallel protons appeared immediately when sc4 encountered the reconnected field line, consistent more with the local DMC source than reflected bow shock source. This further demonstrates that the formation of the DMC is controlled by magnetic reconnection, which generates freshly reconnected flux tubes that subsequently end up as stagnant fossil flux tubes in the DMC that had reconnected some time ago. So the extended DMCs are formed by various reconnected flux tubes, where the newly generated flux is modifying the existing DMC. It is shown here that when IMF was first northward the DMC formed more tailward and as IMF turned southward the new cavity formed more sunward but overlapping with the old cavity as sc3 remained in the cavity the entire time.

[77] 8. The large-amplitude "turbulence" observed in the cavity can be a consequence of spacecraft crossing flux tubes generated by the reconnection process (see, for example, fluctuating magnetic field during reconnection intervals in Figures 5, 8, and 9) and back and forth motion of the boundaries over the spacecraft (see repeated transitions for sc1 from magnetosphere to cavity due to dynamic pressure variations of solar wind at 1845–1905 UT in Figure 2). Three things can contribute to this relative motion over the flux tubes: (1) spacecraft motion, (2) flux tube motion, and (3) motion of the entire DMC due to highly variable dynamic pressure of the solar wind. The more detailed description on the analysis of magnetic field fluctuations in the cavity is given by *Nykyri et al.* [2011].

[78] The origin of high-energy particles in the cusp diamagnetic cavities has been a long-standing and controversial topic. The present study does not exclude the bow shock or magnetospheric source for energetic ions but rather adds new constraints to these sources:

[79] 1. At the very close vicinity to the DMC boundary there are some particles streaming parallel but also antiparallel to magnetosheath field lines. If the antiparallel energetic population is on the magnetosheath field line that has not yet reconnected these particles cannot directly originate from quasi-parallel bow shock.

[80] 2. The region of energetic protons forms a very narrow layer at the magnetosheath close to DMC boundary characterized by butterfly shape distribution function at high energies continuing to antiparallel direction. This signature in the magnetosheath can be caused by the leakage of energetic particles to the magnetosheath due to their large gyroradius. The fact that fluxes of high-energy (20–40 keV) O+ are observed during most of the magnetosheath crossing at very oblique pitch angles is also consistent with DMC source, since the O+ has larger gyroradius than H+.

[81] 3. Because the field in the DMC is weak, the loss cone into the magnetosheath and magnetosphere is small. Therefore, the adiabatic access from magnetosheath or

magnetosphere would not explain the trapped population with closely perpendicular pitch angles observed in the cavity.

[82] 4. Previous studies [e.g., *Chang et al.*, 1998, 2000; *Trattner et al.*, 2001] have not quantitatively shown the width of the magnetosheath layer surrounding the DMC that maps to the quasi-parallel bow shock. Determining the width of this layer along the cavity boundary normal direction is important as it would help clarify the energetic ion source: if this width is wider than the gradients, L (for example, sc1 and sc4 separation along boundary normal at ~1924 UT is around 1200–2470 km), calculated in this paper (Tables 3 and 4), then the high-energy particle fluxes should not drop in distance L (see Nykyri et al., submitted manuscript, 2010), if the energetic ion source for the DMC is the quasi-parallel bow shock.

[83] 5. Bow shock source does not explain the energetic electrons (see Figure 4, top) and O+ ions (see second panel in Figure 12) observed in the cavity.

[84] Our detailed analysis of high-energy particle observations from RAPID instrument during this event implies even stronger constraints for magnetospheric and magnetosheath sources (Nykyri et al., submitted manuscript, 2010). Based on these constraints the most simple explanation on the origin for high-energy particles observed in the DMC is the local source. We will also discuss the acceleration mechanism that works both for electrons and protons in the work by Nykyri et al. (submitted manuscript, 2010).

Appendix A: Example Calculation of Boundary Normals and Error Estimates

[85] Examination of the Cluster data indicates that boundary crossings and areas surrounding the crossings at the high-altitude cusp are not smooth but show fluctuations at different frequencies. Therefore the calculations of the boundary normals are sensitive to the length of the window that is used in variance analysis. In order to test the time stationarity and calculate the error estimates of the MVAB, MVAE and MFR normals and normal component of B field we have utilized a technique described by *Sonnerup and Scheible* [1998]. Figure A1a illustrates an example of a calculation of a reference normal using MVAB, MVAE and MFR tests, Figure A1b shows time stationarity of MVAE normals measured by sc1 during a current sheet crossing centered at 1918:30 UT, and Figure A1c shows spacecraft separations along sc1 plateau normals. Figures A1b (middle) and A1b (bottom) show the angular deviations, $\Delta\phi_{13}$ and $\Delta\phi_{12}$ (in radians) between individual normal x_1 and the reference normal $x_1' = [0.66, 0.44, 0.61]$ toward x_3' and x_2', respectively, where the set (x_1', x_2', x_3') is specified in Figure A1a (middle). The Plateau (light blue column) is

Figure A1. (a) Hodograms, eigenvectors, and eigenvalues of MVAB, MVAE, and MFR analysis during reference interval 1917:00–1919:30 UT. The MVAE maximum eigenvector (reference normal) and λ_1/λ_2 ratio are highlighted in pink. (b) Stationarity of MVAE normals calculated during nested segments around 1918:30 UT: Figure A1b (top) shows the normal component of the magnetic field, and the quantities 13 and 12 indicate angular deviations (in radians) from the reference normal x1′ = [0.66, 0.44, 0.61] toward x3′ and x2′, respectively, where the set (x1′, x2′, x3′) is specified in Figure A1a (middle). The plateau is defined as an interval having the smallest angular deviations and constant normal component of magnetic field and is highlighted with light blue. (c) Projected spacecraft distances (in km) along plateau normals. For example, average distance between sc3 and sc4 along the measured plateau normals is 6057 km.

a)

Cluster 2003.02.14

Magnetic Field Variance   Variance Interval 19.2833 - 19.3333

Eigenvectors:
j = 0.6730
    -0.6606
    -0.3328

Eigenvalue Ratios:
Max/Int: 3.09
Int/Min: 3.27

k = 0.2676
    0.6369
    -0.7230

i = 0.6896
    0.3975
    0.6054

✳ - Initial Point
○ - Final Point

Electric Field Variance

Eigenvectors:
j = 0.6559
    0.4394
    0.6138

Eigenvalue Ratios:
Max/Int: 7.53
Int/Min: 2.51

k = 0.3819
    0.5082
    -0.7720

i = -0.6511
    0.7407
    0.1655

MVAE Ref. normal

Minimum Faraday Residue

Eigenvectors:
j = 0.7472
    -0.5023
    -0.4352

Eigenvalue Ratios:
Max/Int: 1.56
Int/Min: 3.95

k = 0.0837
    0.7208
    -0.6881

i = 0.6593
    0.4777
    0.5806

MVAB, MVAE and MFR Variance and Eigenvectors during
Reference Interval: 19:17:00 - 19:20:00 UT

b) Stationarity of MVAE normals of Sc1 centered at 19:18:30

Plateau

Reference Interval: 19:17:00–19:20:00
Reference Normal: 0.656, 0.440, 0.614

c) Spacecraft separations along plateau normals of Sc1

Avg. dist. along plateau normals =   447.5

Avg. dist. along plateau normals =   4944.8

Avg. dist. along plateau normals =   1112.1

Avg. dist. along plateau normals =   1559.6

Avg. dist. along plateau normals =   4497.3

Avg. dist. along plateau normals =   6056.9

Average Plateau Normal: 0.670, 0.431, 0.604
Average Plateau Eigenvalue Ratio: 6.821

Figure A1

$$y'_1 = |x_3|\sin(\theta)\sin(\varphi) = x_3 \bullet x'_1$$
$$y'_2 = |x_3|\cos(\theta) = x_3 \bullet x'_2$$
$$y'_3 = |x_3|\sin(\theta)\cos(\varphi) = x_3 \bullet x'_3$$
$$|x_3| = 1$$
$$\theta = \cos^{-1}(x_3 \bullet x'_2)$$
$$\cos(\varphi) = \frac{x_3 \bullet x'_3}{\sin(\theta)} \Rightarrow$$
$$\Delta\varphi_{31} = \varphi = \cos^{-1}\left(\frac{x_3 \bullet x'_3}{\sin(\cos^{-1}(x_3 \bullet x'_2))}\right)$$

Figure A2. Illustration of calculation of $\Delta\phi_{13}$: deviation between individual normal x_3 and the reference normal x'_3 toward x'_1.

defined as a region having approximately a constant normal component of the magnetic field and smallest $\Delta\phi_{13}$ and $\Delta\phi_{12}$ values. For MFR and MVAB tests the deviation between individual normal x_3 and the reference normal x'_3 toward x'_1 is calculated as

$$\Delta\phi_{31} = \cos^{-1}\left(\frac{x_3 \cdot x'_3}{\sin(\cos^{-1}(x_3 \cdot x'_2))}\right) \tag{A1}$$

with error bars calculated from

$$\sqrt{\frac{\lambda_3\lambda_1}{(m-1)(\lambda_3-\lambda_1)^2}} \tag{A2}$$

[86] Figure A2 illustrates the calculation of $\Delta\phi_{31}$. Deviation toward x'_2 and error bars are calculated from

$$\Delta\phi_{32} = \cos^{-1}\left(\frac{x_3 \cdot x'_3}{\sin(\cos^{-1}(x_3 \cdot x'_1))}\right), \quad \sqrt{\frac{\lambda_3\lambda_2}{(m-1)(\lambda_3-\lambda_2)^2}} \tag{A3}$$

[87] For MVAE test the deviation from x'_1 toward x'_3 and error bars are calculated as

$$\Delta\phi_{13} = \cos^{-1}\left(\frac{x_1 \cdot x'_1}{\sin(\cos^{-1}(x_1 \cdot x'_2))}\right), \quad \sqrt{\frac{\lambda_1\lambda_3}{(m-1)(\lambda_1-\lambda_3)^2}} \tag{A4}$$

[88] Deviation toward x'_2 with error bars are calculated from

$$\Delta\phi_{12} = \cos^{-1}\left(\frac{x_1 \cdot x'_1}{\sin(\cos^{-1}(x_1 \cdot x'_3))}\right), \quad \sqrt{\frac{\lambda_1\lambda_2}{(m-1)(\lambda_1-\lambda_2)^2}} \tag{A5}$$

[89] The MVAB and MFR error bars for the normal component of the magnetic field are calculated from

$$|\Delta\langle\mathbf{B}\cdot\mathbf{x_3}\rangle| = \sqrt{\frac{\lambda_3}{m-1} + (\Delta\phi_{32}\langle\mathbf{B}\rangle\cdot\mathbf{x_2})^2 + (\Delta\phi_{31}\langle\mathbf{B}\rangle\cdot\mathbf{x_1})^2} \tag{A6}$$

and the MVAE error bars for the normal component of the magnetic field are

$$|\Delta\langle\mathbf{B}\cdot\mathbf{x_1}\rangle| = \sqrt{\frac{\lambda_1}{m-1} + (\Delta\phi_{12}\langle\mathbf{B}\rangle\cdot\mathbf{x_2})^2 + (\Delta\phi_{13}\langle\mathbf{B}\rangle\cdot\mathbf{x_3})^2} \tag{A7}$$

where $\langle\mathbf{B}\rangle$ is the average magnetic field vector during interval.

References

Asikainen, T., and K. Mursula (2005), Energetic particle fluxes in the exterior cusp and the high-latitude dayside magnetosphere: Statistical results from the Cluster/RAPID instrument, *Ann. Geophys.*, 23, 2217–2230.

Asikainen, T., and K. Mursula (2006), Reconnection and energetic particles at the edge of the exterior cusp, *Ann. Geophys.*, 24, 1949–1956.

Balogh, A., et al. (2001), The Cluster magnetic field investigation: Overview of in-flight perfomance and initial results, *Ann. Geophys.*, 19, 1207–1217.

Berchem, J., and C. T. Russell (1982), Magnetic field rotation through the magnetopause: ISEE 1 and 2 observations, *J. Geophys. Res.*, 87, 8139–8148.

Burch, J. L. (1973), Rate of erosion of dayside magnetic flux based on a quantitative study of the dependence of polar cusp latitude on the interplanetary magnetic field, *Radio Sci.*, 8, 955–961.
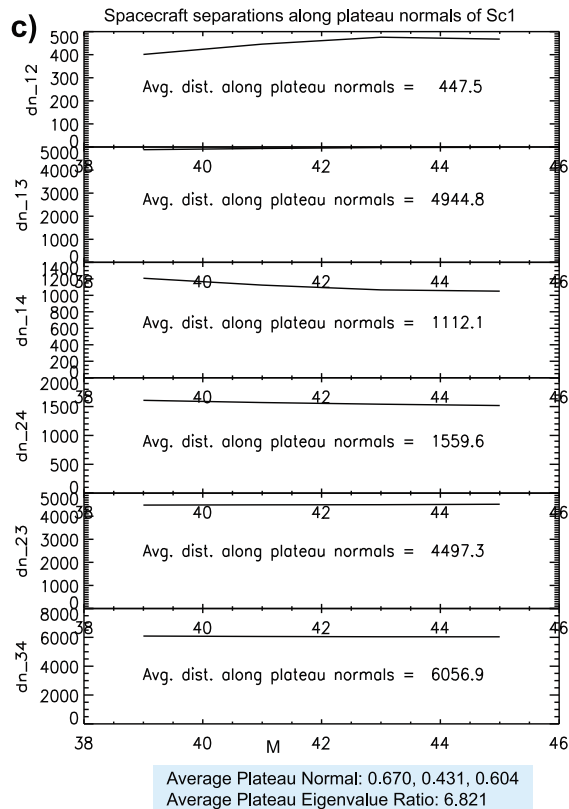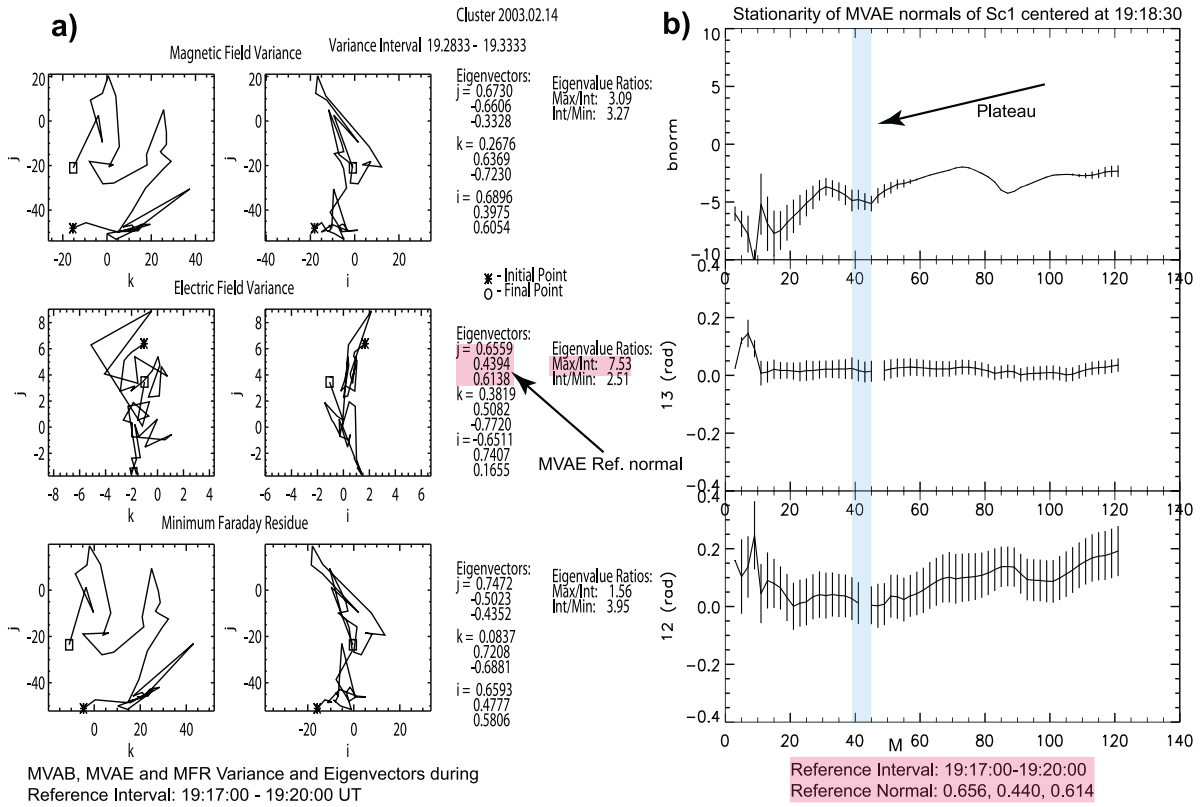
Cargill, P. J., M. W. Dunlop, B. Lavraud, R. C. Elphic, D. L. Holland, K. Nykyri, A. Balogh, I. Dandouras, and H. Réme (2004), CLUSTER encounters with the high altitude cusp: Boundary structure and magnetic field depletions, *Ann. Geophys.*, 22(5), 1739–1754.

Cargill, P. J., et al. (2005), *The Cusp, Outer Magnetospheric Boundaries: Cluster Results*, Int. Space Sci. Inst., Bern.

Chang, S., et al. (1998), Cusp energetic ions: A bow shock source, *J. Geophys. Res.*, 25, 3729–3732.

Chang, S., et al. (2000), Energetic magnetosheath ions connected to the Earth's bow shock: Possible source of cusp energetic ions, *J. Geophys. Res.*, 105, 5471–5488.

Chen, J. (2008), Evidence for particle acceleration in the magnetospheric cusp, *Ann. Geophys.*, 26, 1993–1997.

Chen, J. S., and T. A. Fritz (1998), Correlation of cusp MeV helium with turbulent ULF power spectra and its implications, *Geophys. Res. Lett.*, 25, 4113–4116.

Chen, J., and T. A. Fritz (2001), Energetic oxygen ions of ionospheric origin observed in the cusp, *Geophys. Res. Lett.*, 28, 1459–1462.

Delcourt, D. C., and J. Sauvaud (1998), Recirculation of plasma sheet particles into the high-latitude boundary layer, *J. Geophys. Res.*, 103, 26,521–26,532.

Dunlop, M. W., P. J. Cargill, T. J. Stubbs, and P. Woolliams (2000), The high altitude cusps: HEOS 2, *J. Geophys. Res.*, 105, 27,509–27,517.

Frank, L. A., and K. L. Ackerson (1971), Observations of charged particle precipitation into the auroral oval, *J. Geophys. Res.*, 76, 3612–3643.

Fritz, T., J. Chen, R. Sheldon, H. Spence, J. Fennell, S. Livi, C. Russell, and J. Pickett (1999), Cusp energetic particle events measured by POLAR spacecraft, *Phys. Chem. Earth C*, 24, 135–140.

Fuselier, S. A., D. M. Klumpar, and E. G. Shelley (1991), On the origins of energetic ions in the Earth's dayside magnetosheath, *J. Geophys. Res.*, 96, 47–56.

Fuselier, S. A., K. J. Trattner, and S. M. Petrinec (2000), Cusp observations of high- and low-latitude reconnection for northward interplanetary magnetic field, *J. Geophys. Res.*, 105, 253–266.

Gosling, J. T., M. F. Thomsen, S. J. Bame, R. C. Elphic, and C. T. Russell (1991), Observations of reconnection of interplanetary and lobe magnetic field lines at the high-latitude magnetopause, *J. Geophys. Res.*, 96, 14,097–14,106.

Haaland, S. E., et al. (2004), Four-spacecraft determination of magnetopause orientation, motion and thickness: Comparison with results from single-spacecraft methods, *Ann. Geophys.*, 22, 1347–1365.

Heikkilä, W. J., and J. D. Winningham (1971), Penetration of magnetosheath plasma to low altitudes through the dayside magnetospheric cusps, *J. Geophys. Res.*, 76, 883–891.

Kessel, R. L., S.-H. Chen, J. L. Green, S. F. Fung, S. A. Boardsen, L. Tan, T. E. Eastman, J. D. Craven, and L. A. Frank (1996), Evidence of high-latitude reconnection during northward IMF: Hawkeye observations, *Geophys. Res. Lett.*, 23, 583–586.

Khrabrov, A. V., and B. Sonnerup (1998), Orientation and motion of current layers: Minimization of the Faraday residue, *Geophys. Res. Lett.*, 25, 2373–2376.

Kremser, G., J. Woch, K. Mursula, P. Tanskanen, B. Wilken, and R. Lundin (1995), Origin of energetic ions in the polar cusp inferred from ion composition measurements by the Viking satellite, *Ann. Geophys.*, 13, 595–607.

Lavraud, B., and P. J. Cargill (2005), The magnetospheric cusps revealed: Results from the Cluster mission, *Astron. Geophys.*, 46, 1.32–1.35.

Lavraud, B., et al. (2002), Cluster observations of the exterior cusp and its surrounding boundaries under northward IMF, *Geophys. Res. Lett.*, 29(20), 1995, doi:10.1029/2002GL015464.

Lavraud, B., et al. (2004), The exterior cusp and its boundary with the magnetosheath under northward IMF: Cluster multi-event analysis, *Ann. Geophys.*, 22(8), 3039–3054.

Lavraud, B., et al. (2005a), High-altitude cusp flow dependence on IMF orientation: A 3-year Cluster statistical study, *J. Geophys. Res.*, 110, A02209, doi:10.1029/2004JA010804.

Lavraud, B., et al. (2005b), Cluster observes the high-altitude cusp region, *Surv. Geophys.*, 26, 135–175.

Le, G., X. Blanco-Cano, C. T. Russell, X.-W. Zhou, F. Mozer, K. J. Trattner, S. A. Fuselier, and B. J. Anderson (2001), Electromagnetic ion cyclotron waves in the high-altitude cusp: Polar observations, *J. Geophys. Res.*, 106, 19,067–19,079.

Lyu, L. H., and J. R. Kan (1989), Structures of Alfven shocks: S-shaped magnetic hodogram observed at the magnetopause, *Geophys. Res. Lett.*, 16, 349–352.

Newell, P. T., and C. Meng (1987), Cusp width and B(z): Observations and a conceptual model, *J. Geophys. Res.*, 92, 13,673–13,678.

Niehof, J. T., T. A. Fritz, R. H. W. Friedel, and J. Chen (2008), Interdependence of magnetic field and plasma pressures in cusp diamagnetic cavities, *Geophys. Res. Lett.*, 35, L11101, doi:10.1029/2008GL033589.

Niehof, J. T., T. A. Fritz, R. H. W. Friedel, and J. Chen (2010), Size and location of cusp diamagnetic cavities observed by Polar, *J. Geophys. Res.*, 115, A07201, doi:10.1029/2009JA014827.

Nykyri, K., P. J. Cargill, E. Lucek, T. S. Horbury, A. Balogh, B. Lavraud, I. Dandouras, and H. Rème (2003a), Ion cyclotron waves in the high altitude cusp: CLUSTER observations at varying spacecraft separations, *Geophys. Res. Lett.*, 30(24), 2263, doi:10.1029/2003GL018594.

Nykyri, K., A. Otto, J. Büchner, B. Nikutowski, W. Baumjohann, L. M. Kistler, and C. Mouikis (2003b), Equator-S observations of boundary signatures: FTE's or Kelvin-Helmholtz waves?, in *Earth's Low Latitude Boundary Layer*, *Geophys. Monogr. Ser.*, vol. 133, pp. 205–210, AGU, Washington, D. C.

Nykyri, K., et al. (2004), Cluster observations of magnetic field fluctuations in the high-altitude cusp, *Ann. Geophys.*, 22, 2413–2429.

Nykyri, K., B. Grison, P. J. Cargill, B. Lavraud, E. Lucek, I. Dandouras, A. Balogh, N. Cornilleau-Wehrlin, and H. Réme (2006a), Origin of the turbulent spectra in the high-altitude cusp: Cluster spacecraft observations, *Ann. Geophys.*, 24, 1057–1075.

Nykyri, K., A. Otto, B. Lavraud, C. Mouikis, L. Kistler, A. Balogh, and H. Réme (2006b), Cluster observations of reconnection due to the Kelvin-Helmholtz instability at the dawn side magnetospheric flank, *Ann. Geophys.*, 24, 2619–2643.

Nykyri, K., A. Otto, E. Adamson, and A. Tjulin (2011), On the origin of fluctuations in the cusp diamagnetic cavity, *J. Geophys. Res.*, doi:10.1029/2010JA015888, in press.

Otto, A. (1995), Magnetic reconnection at the magnetopause: A fundamental process and manifold properties, *Rev. Geophys.*, 33, 657–663.

Palmroth, M., P. Janhunen, T. I. Pulkkinen, and W. K. Peterson (2001a), Cusp and magnetopause locations in global MHD simulation, *J. Geophys. Res.*, 106, 29,435–29,450.

Palmroth, M., H. Laakso, and T. I. Pulkkinen (2001b) Location of high-altitude cusp during steady solar wind conditions, *J. Geophys. Res.*, 106, 21,109–21,122.

Paschmann, G., G. Haerendel, N. Sckopke, H. Rosenbauer, and P. C. Hedgecock (1976), Magnetic field characteristics of the distant polar cusp near local noon: The entry layer, *J. Geophys. Res.*, 81, 2883–2899.

Pitout, F., C. P. Escoubet, B. Klecker, and H. Rème (2006), Cluster survey of the mid-altitude cusp: 1. Size, location, and dynamics, *Ann. Geophys.*, 24, 3011–3026.

Rème, H., et al. (2001), First multispacecraft ion measurements in and near the Earth's magnetosphere with the identical Cluster ion spectrometry (CIS) experiment, *Ann. Geophys.*, 19, 1303–1354.

Russell, C. T., G. Le, and S. M. Petrinec (2000), Cusp observations of high-and low-latitude reconnection for northward IMF: An alternate view, *J. Geophys. Res.*, 105, 5489–5495.

Savin, S. P., et al. (1998), The cusp/magnetosheath interface on May 29, 1996: Interball-1 and Polar observations, *Geophys. Res. Lett.*, 25, 2963–2966, doi:10.1029/98GL01402.

Savin, S. P., et al. (2002), Multi-spacecraft tracing of turbulent boundary layer, *Adv. Space Res.*, 30(12), 2821–2830.

Savin, S. P., et al. (2004), Magnetosheath-cusp interface, *Ann. Geophys.*, 22, 183–212.

Scudder, J. D., F. S. Mozer, N. C. Maynard, and C. T. Russell (2002), Fingerprints of collisionless reconnection at the separator, I, Ambipolar-Hall signatures, *J. Geophys. Res.*, 107(A10), 1294, doi:10.1029/2001JA000126.

Sibeck, D. G., R. W. McEntire, A. T. Y. Lui, R. E. Lopez, and S. M. Krimigis (1987), Energetic magnetospheric ions at the dayside magnetopause: Leakage or merging?, *J. Geophys. Res.*, 92, 12,097–12,114.

Sonnerup, B. U. Ö., and M. Scheible (1998), Minimum and maximum variance analysis, in *Analysis Methods for Multi-spacecraft Data*, edited by G. Paschmann and P. W. Daly, *ISSI Sci. Rep., SR 001*, pp. 185–220, Int. Space Sci. Inst., Bern.

Sonnerup, B. U. Ö., G. Paschmann, I. Papamastorakis, N. Sckopke, G. Haerendel, S. J. Bame, J. R. Asbridge, J. T. Gosling, and C. T. Russell (1981), Evidence for magnetic reconnection at the Earth's magnetopause, *J. Geophys. Res.*, 86, 10,049–10,067.

Sonnerup, B. U. Ö., G. Paschmann, and T.-D. Phan (1995), Fluid aspects of reconnection at the magnetopause: In situ observations, in *Physics of the Magnetopause*, *Geophys. Monogr. Ser.*, vol. 90, edited by P. Song, B. U. Ö. Sonnerup, and M. F. Thomsen, pp. 167–180, AGU, Washington, D. C.

Sundkvist, D., et al. (2005), Multi-spacecraft determination of wave characteristics near the proton gyrofrequency in high-altitude cusp, *Ann. Geophys.*, 23, 983–995.

Trattner, K. J., S. A. Fuselier, W. K. Peterson, S.-W. Chang, R. Friedel, and M. R. Aellig (2001), Origins of energetic ions in the cusp, *J. Geophys. Res.*, 106, 5967–5976.

Twitty, C., T. D. Phan, G. Paschmann, B. Lavraud, H. Rème, and M. Dunlop (2004), Cluster survey of cusp reconnection and its IMF dependence, *Geophys. Res. Lett.*, *31*, L19808, doi:10.1029/2004GL020646.

Vontrat-Reberac, A., J. M. Bosqued, M. G. G. T. Taylor, B. Lavraud, D. Fontaine, M. W. Dunlop, H. Laakso, N. Cornilleau-Werhlin, P. Canu, and A. Fazakerley (2003), Cluster observations of the high-altitude cusp for northward interplanetary magnetic field: A case study, *J. Geophys. Res.*, *108*(A9), 1346, doi:10.1029/2002JA009717

Walsh, B. M., T. A. Fritz, N. M. Lender, J. Chen, and K. E. Whitaker (2007), Energetic particles observed by ISEE-1 and ISEE-2 in a cusp diamagnetic cavity on 29 September 1978, *Ann. Geophys.*, *25*, 2633–2640.

Walsh, B. M., T. A. Fritz, M. M. Klida, and J. Chen (2010), Energetic electrons in the exterior cusp: Identifying the source, *Ann. Geophys.*, *28*, 983–992.

Whitaker, K. E., J. Chen, and T. A. Fritz (2006), CEP populations observed by ISEE 1, *Geophys. Res. Lett.*, *33*, L23105, doi:10.1029/2006GL027731.

Whitaker, K. E., T. A. Fritz, J. Chen, and M. Klida (2007), Energetic particle sounding of the magnetospheric cusp with ISEE-1, *Ann. Geophys.*, *25*, 1175–1182.

Wilken, B., et al. (2001), First results from the RAPID imaging energetic particle spectrometer on board Cluster, *Ann. Geophys.*, *19*, 1355–1366.

Zhang, H., T. A. Fritz, Q.-G. Zong, and P. W. Daly (2005), Stagnant exterior cusp region as viewed by energetic electrons and ions: A statistical study using Cluster Research with Adaptive Particle Imaging Detectors (RAPID) data, *J. Geophys. Res.*, *110*, A05211, doi:10.1029/2004JA010562.

Zhou, X. W., C. T. Russell, G. Le, S. A. Fuselier, and J. D. Scudder (1999), The polar cusp location and its dependence on dipole tilt, *Geophys. Res. Lett.*, *26*, 429–432.

Zhou, X. W., C. T. Russell, G. Le, S. A. Fuselier, and J. D. Scudder (2000), Solar wind control of the polar cusp at high altitude, *J. Geophys. Res.*, *105*, 245–251.

E. Adamson and A. Otto, Geophysical Institute, University of Alaska Fairbanks, Fairbanks, AK 99775, USA.

E. Dougal, J. Mumme, and K. Nykyri, Department of Physical Sciences, Embry-Riddle Aeronautical University, 600 S. Clyde Morris Blvd., Daytona Beach, FL 32114, USA. (nykyrik@erau.edu)